Accepted Manuscript

Structure, morphology and photoluminescence emissions of $ZnMoO_4$: RE^{3+}=Tb^{3+} - Tm^{3+} - X Eu^{3+} (x = 1, 1.5, 2, 2.5 and 3□mol%) particles obtained by the sonochemica method

L.X. Lovisa, M.C. Oliveira, J. Andrés, L. Gracia, M.S. Li, E. Longo, R.L. Tranquilin, C.A. Paskocimas, M.R.D. Bomio, F.V. Motta

PII: S0925-8388(18)31271-4

DOI: 10.1016/j.jallcom.2018.03.394

Reference: JALCOM 45624

To appear in: *Journal of Alloys and Compounds*

Received Date: 18 January 2018

Revised Date: 19 March 2018

Accepted Date: 29 March 2018

Please cite this article as: L.X. Lovisa, M.C. Oliveira, J. Andrés, L. Gracia, M.S. Li, E. Longo, R.L. Tranquilin, C.A. Paskocimas, M.R.D. Bomio, F.V. Motta, Structure, morphology and photoluminescence emissions of $ZnMoO_4$: RE^{3+}=Tb^{3+} - Tm^{3+} - X Eu^{3+} (x = 1, 1.5, 2, 2.5 and 3□mol%) particles obtained by the sonochemical method, *Journal of Alloys and Compounds* (2018), doi: 10.1016/j.jallcom.2018.03.394.

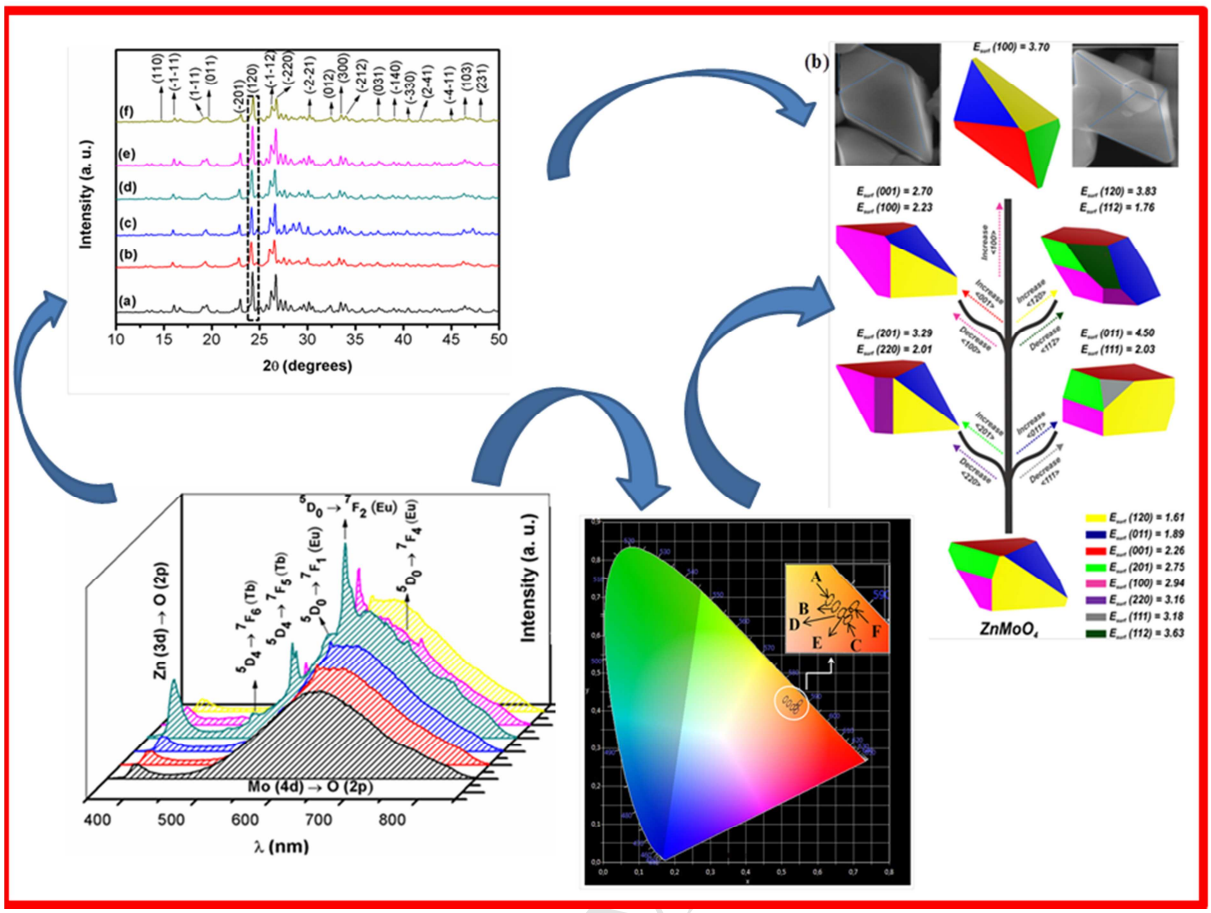

Structure, morphology and photoluminescence emissions of $ZnMoO_4$: RE $^{3+}$=Tb^{3+} - Tm^{3+} - x Eu^{3+} (x = 1, 1.5, 2, 2.5 and 3 mol%) particles obtained by the sonochemical method

L. X. Lovisa[a]*, M. C. Oliveira[b], J. Andrés[b], L.Gracia[c], M. S. Li[d], E. Longo[e], R.L. Tranquilin[a], C. A. Paskocimas[a], M. R. D. Bomio[a] and F.V. Motta[a]

[a]*LSQM—Laboratório de Síntese Química de Materiais, DEMAT, UFRN, Natal, Campus, Lagoa Nova, Natal, RN CEP 59078 ‑900, Brazil*

[b]*Departament de Química Física i Analítica, Universitat Jaume I, Campus del Riu Sec, Castelló E-12071, Spain*

[c]*Department of Química-Física, Universitat de València, 46100 Burjassot, Spain*

[d]*IFSC, USP, Av. Trabalhador São Carlense, 400, CEP 13566-590 São Carlos, SP, Brazil*

[e]*LIEC, IQ, UNESP, Rua Francisco Degni s/n, CEP 14801-907 Araraquara, SP, Brazil*

Abstract:

$ZnMoO_4$ and $ZnMoO_4$: RE^{3+}= 1% Tb^{3+}, 1% Tm^{3+}, x Eu^{3+} (x = 1, 1.5, 2, 2.5 and 3 mol%) particles were prepared by a sonochemical method. The influence of the dopant content on photoluminescent behavior was investigated. The X-ray diffraction results confirmed the formation of the α-$ZnMoO_4$ phase with a triclinic crystalline structure. The influence of the chemical compositions on photoluminescence emissions has been studied and the results clearly show the specific emissions of Tb^{3+} and Eu^{3+}, simultaneously, with a strong contribution of the matrix. Band gap values are in the range of 3.55 to 4.25 eV. From the values calculated for the CIE coordinates, it was observed that this material develops an emission tendency in the orange-red region. It has been demonstrated for the first time that the sample $ZnMoO_4$: 1% Tb^{3+}, 1% Tm^{3+}, 2% molEu^{3+}, presented higher photoluminescence intensity. At higher concentrations of RE^{3+}, the quenching effect was observed. The morphology of samples are interpreted based on a comparative analysis of the calculated and experimental field emission scanning electron microscopy (FE-SEM) images. First-principle calculations at a density functional theory level were performed to obtain the values of surface energies and relative stability of the (120), (001), (011), (201), and (100) surfaces by employing the Wulff construction.A complete map of the available morphologies of $ZnMoO_4$ and $ZnMoO_4$:12.5%molEu^{3+} is obtained and a possible explanation for the transformation processes is provided in which the experimental and theoretical morphologies can match. The present study offers a fundamental knowledge that is expected to enable the fabrication of $ZnMoO_4$-based phosphor materials with a controllable emission peak shift and intensity.

Key words: $ZnMoO_4$: Tb^{3+} - Tm^{3+} - Eu^{3+};Sonochemical method; Photoluminescence

*Corresponding author. Tel: +55-84-3342-2512; Fax: +55-84-3342-2406

E-mail address: lauraengmat@hotmail.com (Lovisa, L. X.)

1. Introduction

Over the last decades, the interest for molybdates has been increasing due to their potential applications in the most diverse areas, such as biology, photoluminescence, photocatalysis, and lithium ion batteries [1-4]. Rare earth cations, RE^{3+}, doped molybdates present high chemical stability, which allows them to be applied in versatile applications, such as plasma display panels, field emission display, lighting industries and white light emitting diodes [5-9].Therefore, these materials are considered a new generation of light sources, which have been replacing fluorescent lamps efficiently, due to low energy consumption and fast response.

The doping processes of RE^{3+}, the main members of lanthanide´s group, at the lattice of the molybdates are responsible for the appearance of optical properties due to 4f valence shell electrons, while photoluminescence emissions are associated to f-f or 4f-5d transitions [10, 11], and the emission wavelength also depends on the splitting of energy level. For example, Eu^{3+} cations are activated phosphors that provoke a strong red emitter signal due to $^5D_0 \rightarrow {}^7F_2$ electric dipole transition [12], while Tb^{3+} cations are activated phosphors which reads a strong green emission due to the transitions of $^5D_3$-^7F_J in the blue and $^5D_4$-^7F_J in the green region (J = 6, 5, 4, 3, 2) and the transition intensities depend on their critical doping concentrations [13].

On the other hand, it is well known that the co-doping process of RE^{3+} is an adequate procedure to enhance intensity since in this process the energy transfer occurs from one RE^{3+}cation which acts as a sensitizer to another RE^{3+}cation acting as activator. Along this process, the energy transfer between RE^{3+}cations is possible due to a plethora of effects such as resonant energy transfer, energy transfer by non-radiative transition and quantum cutting [14]. Many combinations of sensitizer and activator of RE^{3+} were developed as Er^{3+}–Yb^{3+}, Eu^{3+}–Gd^{3+}, Eu^{3+}–Sm^{3+} and Eu^{3+}–Tb^{3+}[15 -21].

For the zinc molybdate, $ZnMoO_4$, as a representative member of molybdate family, recent experimental and theoretical studies have evaluated in detail their phosphorescent behavior at low temperatures and a crystal phosphor model was proposed to explain the corresponding mechanism[22-24]. In addition, the influence of the growth conditions of the $ZnMoO_4$ crystals and the characteristics of the decay are analyzed to find an increase of the luminescence emissions [25]. $ZnMoO_4$ is an

inorganic semiconductor that present two types of crystal structures: alpha (α) and beta (β) and has been successfully synthesized by different methods, including the sonochemistry, precipitation and hydrothermal processes [26-29]. The type of phase obtained depends on the conditions of synthesis, time, and temperature processing [30]. The crystals α-$ZnMoO_4$ have a triclinic structure, with space group $P\bar{1}$ and group symmetry C_1[31], in which the Zn cations are coordinated by six oxygen anions that form the distorted octahedral [ZnO_6], while Mo cations are bound to four oxygen anions in a tetrahedral configuration [MoO_4] [32]. The crystals β-$ZnMoO_4$ have a monoclinic structure of the wolframite type, with space group $P_{2/c}$and group symmetry C_{2h}^4. In the monoclinic structure, the Zn and Mo cations are coordinated by six oxygen atoms that form the distorted octahedral [ZnO_6] and [MoO_6], respectively [33].

Mikhailik et al. [34] proposed that the photoluminescent properties of $ZnMoO_4$ are related to self-localized excitons and to electron transitions within the anionic molecular complex $[MoO_4]^{2-}$. The emission bands can be associated to radioactive recombination processes of the electron-hole pairs located in the anionic molecular complex $[MoO_4]^{2-}$and this moiety is considered the main constituent element, which defines the optical properties in the visible ultraviolet energy region [35].Cavalcante et al. [36] attributed that the differences in photoluminescence emission intensities of $ZnMoO_4$ microcrystals are due to the presence of changes in the particle morphology, crystal size and surface defects. RE^{3+} doped $ZnMoO_4$, $ZnMoO_4$:RE^{3+}, have been widely investigated for possible application in optical devices. According to Ju et al. [37], in their work with $ZnMoO_4$: Tb from the co-precipitation method, concluded that the light flux in green is more significant than in red and blue among materials co-doped due to the intense emission of the $^5D_4 \rightarrow {}^7F_5$ (Tb^{3+}) at 550 nm and that this type of material exhibits excellent thermal and chemical stability [38-40]. Chengaiah et al. [41] evaluated the effect of Dy^{3+} dopant concentration on the $ZnMoO_4$ matrix and observed a mixture of emissions in the yellow and blue regions. Through the determination of the chromaticity coordinates, it was possible to produce a material with emission in white. Ran et al. [42] have already described that the energy transfer efficiency between the Bi^{3+} sensitizer and the Eu^{3+} activator in the $ZnMoO_4$ matrix is associated with the concentration of the dopants and the distance between them, highlighting their performance as photoluminescent material in the use of LEDs white.

In this work, a series of the $ZnMoO_4$ and $ZnMoO_4$: 1% Tb^{+3}, 1% Tm^{+3}, x Eu^{+3} (x = 1, 1.5, 2, 2.5 and 3 mol %) particles were prepared by the sonochemical for the preparation of the $ZnMoO_4$ and $ZnMoO_4$: 1% Tb^{+3}, 1% Tm^{+3}, x Eu^{+3} (x = 1, 1.5, 2, 2.5 and 3 mol%).The synthesized samples were characterized by X-ray diffraction and Rietveld refinements, field emission scanning electron microscopy (FE-SEM) and photoluminescence emissions. They present photoluminescence (PL) emissions and a tunable band gap in the visible light region. The geometries, electronic structures and properties of both $ZnMoO_4$ and $ZnMoO_4$: 12.5 % Eu^{3+}systems have been characterized and discussed in relation to their crystal structural characteristics by using the density functional theory (DFT)-based calculations. Next, a joint experimental and theoretical strategy, developed by us, was employed to obtain a complete map of the morphologies available for both systems. Based on these results, and by changing the values of the energy surfaces of (120), (011), (001), (201),(220), (100), (111) and (112) surfaces, we are able to rationalize the different path followed for these system by which the experimental FE-SEM images and theoretical morphologies can match.

The remainder of this paper is organized as follows: Section 2 describes the experimental procedure and computational details, Section 3 exhibits the computational details; Sections 4 and 5 present the results and conclusions, respectively.

2. Experimental procedure and computational details

2.1. Materials

Acid Molybdic (H_2MoO_4), (Alfa Aesar), zinc nitrate ($Zn(NO_3)_2.6H_2O$) (Synth), europium oxide (Eu_2O_3) (Alfa Aesar), terbium oxide (Tb_4O_7) (Aldrich), thulium oxide (Tm_2O_3), nitric acid (Synth), ammonium hydroxide (NH_4OH) (Synth) and distilled water were used as received to prepare the $ZnMoO_4$ and $ZnMoO_4$: RE^{3+} particles.

2.2 Preparation

Initially, the oxides (Eu_2O_3, Tb_4O_7 and Tm_2O_3) were dissolved separately in 10 ml of nitric acid to obtain their respective nitrates. Since in the form of oxides, these elements are insoluble in the reaction medium. For the synthesis of the $ZnMoO_4$ and $ZnMoO_4$: RE^{3+} particles, two precursor solutions were prepared: one of molybdenum (solution **A**) and the other of zinc (solution **B**). For the two solutions, the starting reagent was dissolved in 40 ml of distilled water. Solution **A** was exposed to high

intensity ultrasound irradiation at 65% amplitude in continuous mode. Then solution **B** was added to solution A during the ultrasound by dripping in the time interval of every 10 minutes. After the complete dissolution, the dopants (RE^{3+}:Tb^{3+}, Tm^{3+} and Eu^{3+}) in nitrate form were added to the system. Finally, NH_4OH was added to the solution to stabilize the pH at 8. The solution was centrifuged three times in distilled water and then kept in the oven at a temperature of 80°C for 24 hours for drying. The particles were calcined at 650°C for 4 hours at a heating rate of 10°C/minute.

2.3 Characterization

The $ZnMoO_4$ and $ZnMoO_4$:RE^{3+} particles were structurally characterized by XRD using a Shimadzu XRD 7000 instrument with Cu-Kα radiation (λ = 1.5406 Å) in the 2θ range from 10 to 50º at a scanning rate of 0.02^o s^{-1}. The morphologies were investigated using field-emission gun scanning electron microscopy (FEG-SEM; Carl Zeiss, Supra 35- VP Model, Germany) operated at 6 kV. **The chemical analyzes were performed on the equipment of Energy Dispersive X-ray Fluorescence Spectrometer EDX-720- Shimadzu**. The UV-vis diffuse reflectance spectrum was measured at room temperature using a UV-vis spectrometer. The photoluminescence (PL) spectra were acquired with an Ash Monospec 27 monochromator (Thermal Jarrel, U.S.A.) and a R4446 photomultiplier (Hamamatsu Photonics, U.S.A.). The 350 nm beam of a krypton ion laser (Coherent Innova 90 K) was used as the excitation source while its maximum output power was kept at 200 mW. All measurements were performed at room temperature. **The time decay measurements were performed on the equipment Fluorolog3 Horiba Jobin Yvon spectrofluorometer equipped with Hamamatsu R928P photomultiplier, SPEX 1934 D phosphorimeter, and a pulsed 150W Xe-Hg lamp.**

2.4 Computational details

Bulk and surfaces of $ZnMoO_4$ and $ZnMoO_4$:12.5% mol Eu^{3+} were calculated by means of the hybrid functional B3LYP within the periodic density functional theory (DFT) framework [34, 35], using the CRYSTAL14 software package [36].Eu center was represented by a small-core efective-core pseudopotential (ECP)[46], while Mo center was described by a Hay–Wadt type (basis[HAYWSC]-31G) [47]. Oxygen [48] and zinc [49] centers were both represented by standards at 6-31G* basis sets.

In the bulk and surface calculations, the exchange–correlation contribution is the result of a numerical integration of the electron density and its gradient, performed over a grid of points. Default values of the tolerances that control the Coulomband exchange series were adopted (ITOL1 = ITOL2 =ITOL3 = ITOL4 = 8, ITOL5 = 14).The Hamiltonian matrix was diagonalized[50], using 36 reciprocal lattice points *(k*-points), corresponding to a shrinking factor of IS = 4 method for bulk, while 10 *k*-points grids were used for surfaces. In this work, a triclinic supercell of 144 and 143 atoms which corresponds to 1x2x2 conventional cell, was used to simulate the $ZnMoO_4$ and $ZnMoO_4$:12.5% Eu^{3+}, respectively. It is important to note that for the calculation of the doped materials, $ZnMoO_4$:RE^{3+}, we have a technical problem, i.e. because the % of doping is very small, in the range of 1-3 mol%, it is necessary to use very large unit cells. This fact makes calculations computationally very costly, and it was possible to reach a minimum of doping of 12.5% Eu^{3+}.

Slab models for (120), (011), (001), (201),(220), (100), (111) and (112)surfaces were considered to obtain the surface energy, E_{surf}, values and the morphologies of the $ZnMoO_4$ and $ZnMoO_4$: 12.5% Eu^{3+} systems. Surface calculations were determined from the equilibrium shape by a classic Wulff construction[51] that minimizes the total surface free energy at a fixed volume, providing a simple correlation between the E_{surf} of the (*hkl*) plane and the distance, r (*hkl*),in the normal direction from the center of the crystallite. The Wulff construction has been successfully used in materials science to obtain the morphology of materials, including $PbMoO_4$, α-Ag_2MoO_4 as well as $BaMoO_4$ materials[52 - 54].

E_{surf} is defined as the total energy per repeating slab cell (E_{slab}) minus the total energy of the perfect crystal per molecular unit ($E_{bulk/atom}$) multiplied by the number of molecular units of the surface (N_s) and divided by the surface area (A) per repeating cell of the two sides of the slab, as shown in equation (1).

$$E_{suf}=\frac{1}{2A}(E_{slab}- Ns\cdot E_{bulk/atom}) \quad (1)$$

4. Results

The XRD pattern presented in Figure 1 show the diffraction peak characteristics of $ZnMoO_4$. They can be indexed in a triclinic structure of the α type with space group $P\bar{1}$in C_1 symmetry (JCPDS- 35-0765). The XRD patterns of the samples showed that

the $ZnMoO_4$:RE are structurally related to the triclinic crystalline phase. There was no secondary phase formation, indicating that doping occurred successfully.

Insert Figure 1

Figure 1. X-ray diffraction of the $ZnMoO_4$ materials synthesized by the sonochemical method: (a) $ZnMoO_4$, and $ZnMoO_4$: 1% Tb^{3+}, 1% Tm^{3+}, x Eu^{3+} % mol: (b) x= 1%, (c) x= 1.5%, (d) x= 2%, (e) x= 2.5% and (f) x= 3% mol.

A decrease in the intensity of the peak (120) at 24.30° is observed in Figure 1 accompanied by an increase of the amount of dopants in the $ZnMoO_4$ matrix. The structural and electronic distortion in the [ZnO_6] clusters caused by the substitution of $RE^{3+} \rightarrow Zn^{2+}$in the structure of $ZnMoO_4$ is evidenced by the displacement of the peaks to a region of smaller angle according to Figure 1. This fact can be associated to the difference in the size between the $RE^{3+}$and Zn^{2+}cations. Ju et al. [37] noted that the peaks of the XRD patterns become weak and slightly broad due to the increase of the concentration of Tb^{3+}in $ZnMoO_4$.

The values of the mean crystallite size and the micro strain of $ZnMoO_4$ and $ZnMoO_4$:$RE^{+3}$are shown in Table 1. The mean crystallite size was estimated by the Scherrer equation (2)[55].

$$D_{hkl} = {}^{0.9\lambda}/_{\beta Cos\theta} \qquad (2)$$

Where D_{hkl} is the mean crystallite size, λ is the wavelength, θ is half the Bragg angle and β is the half height of the selected reflection (FWHM). The reduction in the crystallite size is verified when the dopant concentration is increased as shown in Figure 2. This behavior is first of all due to the distortion caused in the $ZnMoO_4$ lattice by the dopants, which can slow down the growth of the crystals [56]. According to Vidya et al [57], the dopant provides a lagging force in the grain boundaries. If this generated retarding force is greater than the grain growth force by the formed ion of the lattice (Zn), then the diffusibility is reduced. The micro strain is associated to the synthesis conditions that the materials were formed. For example, the fast precipitation of the $ZnMoO_4$ particles due to the strong attraction force between Zn^{2+}or RE^{3+} and $(MoO_4)^{2+}$ ions due to the addition of NH_4OH. The bonds that form later can generate defects and deformation in the crystals.

Insert Figure 2

Figure 2. Relationship between crystallite size and microdeformation according to RE^{3+} concentration.

The Rietveld refinement method was used to explain possible differences in the structural arrangements induced by the processing of $ZnMoO_4$ and $ZnMoO_4$:RE^{3+} particles. This refinement was performed by using the general structure analysis Maud program version 2.0. The results of the Rietveld refinements are shown in Figure 3. The measured diffraction patterns are well matched to ICSD 1528282. The diffractogram corresponding to the experimental and theoretically calculated data are practically identical, as shown in the Calc-Obs line. The results of the refinement are summarized in Table 1. The high quality of the refinement is revealed by the reliability parameters (X^2, *Rwp*and*Rp*). The Rietveld method uses the profiles of the intensities obtained by the slow scan measurements of the material from the X-ray diffraction technique.

Insert Figure 3

Figure 3. Structural refinement of the samples (a) $ZnMoO_4$, and $ZnMoO_4$: 1% Tb^{3+}, 1% Tm^{3+}, x Eu^{3+} % mol: (b) 1%, (c) 1.5%, (d) 2%, (e) 2.5% and (f) 3% mol.

Table 1. Crystallographic data of $ZnMoO_4$ and $ZnMoO_4$:RE^{3+} samples

Samples	$ZnMoO_4$	$ZnMoO_4$ (Theoretical)	$ZnMoO_4$: 1% Tb 1% Tm 1% mol Eu^{3+}	$ZnMoO_4$: 1% Tb 1% Tm 1.5% mol Eu^{3+}	$ZnMoO_4$: 1% Tb 1% Tm 2% mol Eu^{3+}	$ZnMoO_4$: 1% Tb 1% Tm 2.5% mol Eu^{3+}	$ZnMoO_4$: 1% Tb 1% Tm 3% mol Eu^{3+}
a (Å)	9.6822	9.7476	9.6835	9.69991	9.69056	9.70418	9.70166
b (Å)	6. 9487	6.9847	6.9518	6.95539	6.96208	6.96021	6.96096
c (Å)	8.3687	8.3984	8.3551	8.3668	8.37362	8.37270	8.37684
V (Å)^3	563.0352	526.5936	562.127	564.4800	564.9384	565.5183	565.7120
α	101.7090	101.3339	101.720	101.6817	101.7214	101.7112	101.6878
β	96.7422	96.8497	96.847	96.8367	96.7110	96.82299	96.81503
θ	106.86	106.9862	106.851	106.8180	106.8245	106.8004	106.8083
D (nm)	95.448	-	93.570	93.570	68.839	68.736	67.342
$\mathcal{E}$ *(10*$^{-3}$*)*	1.06	-	1.09	1.16	1.32	2.24	2.9
Rwp	6.80	-	8.05	6.93	10.03	8.37	8.54
Rb	3.80	-	11.27	12.21	7.49	13.17	6.83
χ^2	0.56	-	1.40	1.28	0.72	1.50	0.80

The cell and atomic position parameters used in the calculations are taken from the results of the Rietveld refinements for both structures (Table 1). An optimization of the cell parameters was performed and the unit cell representation was modeled using a single conventional 1×2×2 cell for $ZnMoO_4$ and $ZnMoO_4$:Eu^{3+} materials. The X-Window Crystalline Structures and Densities (XCrySDen) program[58] were used to design the periodic model, as showed in Figure 4(a-b).

Insert Figure 4

Figure 4. Theoretical representation of the triclinic 1x2x2 supercell corresponding to (a) $ZnMoO_4$ and (b) $ZnMoO_4$:12.5% molEu^{3+} crystals.

The determination of the value of the gap energy (Egap) for the $ZnMoO_4$:RE^{3+} particles was performed from the UV-Visible spectroscopy by the diffuse reflectance mode. The obtained reflectance data were converted to absorbance [F(R) = α], generating an absorbance versus energy (eV) plot as indicated in Figure 5. The values of Egap were obtained from the linear extrapolation following the Tauc and Wood method [50].

The electronic transitions in the materials happen through the energy bands and are followed by the emission or absorption of photons in the crystal. For a crystal to have direct electronic transitions, it is necessary to observe the conservation of energy and momentum in the crystal. This condition is favored when the maximum of the valence band (VB) and the minimum of the conduction band (CB) are in the same region of symmetry of the solid. According to different authors [35, 59, 60], the $ZnMoO_4$crystals exhibit an optical absorption spectrum governed by direct electronic transitions. We calculated and plotted the band structure of $ZnMoO_4$ and $ZnMoO_4$: 12.5% molEu^{3+} along various high-symmetry directions in the first Brillouin zone as shown in Figure 6(a-b).An analysis of the results displayed in this Figure points out that the doping of Eu^{+3} provokes a decrease of the values for the energy levels belonging to CB with respect to pure $ZnMoO_4$; the energy range is 5.5-6.0 eV and 2-7-3.6 eV for $ZnMoO_4$ and $ZnMoO_4$: 12.5% mol Eu^{3+}, respectively; while the distribution of energy levels within both CB and VB are more compact at $ZnMoO_4$with respect to $ZnMoO_4$: 12.5% mol Eu^{3+}.

Insert Figure 5

Figure 5. Determination of the gap energy value by using the Tauc and Wood method: (a) $ZnMoO_4$ and $ZnMoO_4$: 1% Tb^{3+}, 1% Tm^{3+}, x Eu^{3+}% mol: (b) x= 1%, (c) x= 1.5%, (d) x= 2%, (e) x= 2.5% and (f) x= 3% mol.

Insert Figure 6

Figure 6. Band structure of (a) $ZnMoO_4$ and (b) $ZnMoO_4$:12.5 molEu^{3+} crystals.

The experimental values found for E_{gap} are in the range of3.55 and 4.25 eV, while theoretical calculations predict an indirect gap of 5.28 and 2.67eV for $ZnMoO_4$ and ZnMoO:Eu^{3+}(12.5%) systems, respectively. Figure 6a-b reveals that the indirect transition is produced along the *k*-points F →G (010 to 001) from the top of VB to the bottom of CB, although the band structure for the doped system is very flat. The projected total DOS for $ZnMoO_4$ and $ZnMoO_4$:12.5% molEu^{3+} are presented in Figures7a and 7b, respectively. An analysis of these figures shows that the VB from 0 to -0.67eV ($ZnMoO_4$) and from 0 to -0.89eV ($ZnMoO_4$: 12.5 % molEu^{3+}) are composed mainly of O orbitals (px,py and pz). CB is mainly formed by the Mo and Eu orbitals with a lower contribution of the Zn orbitals (dz^2, dx^2-y^2, dxy, dxz, dyz), located in the range from 5.28 to 6.07eV ($ZnMoO_4$) and from 2.67 to 3.57eV ($ZnMoO_4$: 12.5 % molEu^{3+}).

Insert Figure 7

Figure 7. Projected total DOS of (a) $ZnMoO_4$ and (b) $ZnMoO_4$: 12.5 % molEu^{3+}.

The substitution of the RE^{3+} cations by Zn^{2+} cations promotes an unbalance in the charges within the crystalline structure of $ZnMoO_4$ because the oxidation states of the cations are different. As a way of restoring material neutrality, structural defects occur. The RE^{3+} cations when incorporated to the $ZnMoO_4$ matrix causes an excess of positive charges, then, Zn^{2+} vacancies appear [41,61, 62]. From an electronic perspective, the presence of these defects promotes the presence of intermediate electronic levels in the forbidden region. This new band gap configuration contributes to electronic transitions occurring at a lower energy level. Figure S1(of Supporting Information)represents the decrease in the Egap with increasing dopant concentration. It is observed that there is no linearity in the relationship between the two parameters. It is

reasonable to consider that other factors may interfere, such as the synthesis method as well as the morphology of the particles.

Figure 8 presents the photoluminescence emission spectrum of the $ZnMoO_4$ and $ZnMoO_4$:RE^{3+}particles. The samples were excited by a laser of λ = 350 nm at room temperature. An analysis of the results displayed in Figure 8 renders a first band of lower intensity located between 370 and 419 nm, which can be associated to the recombination of the hole– electron pairs within the clusters $[ZnO_6]$ with predominant emission in violet. A second band of higher intensity is observed located between 475 nm and 850 nm with a peak at 640 nm. Sczancoski et al. [35] consider that the energy states of the molybdate crystals are formed by oxygen states (2p) located above the VB and molybdenum states (4d) located under the CB as shows in Figure 7. The electronic transitions of type Mo (4d) → O (2p) may present different emissions according to the positioning of the holes in the band structure. This second band was decomposed into four emission bands indicating the contribution of each band of the visible spectrum to the photoluminescence behavior, according to the deconvolutions shown in Figure 9. The transition corresponding to the first deconvolution band is associated with the shallow holes (near the VB) related to O 2p orbitals with dominance in green. While the orange, red and infrared emissions, corresponding to the second, third and fourth bands, are associated to the deep holes (slightly away from theVB) connected to the O 2p orbital [63].

Wu et al. [64] pointed out that the active vibration modes of the Jahn-Teller T_2 symmetry effect may influence the $[MoO_4]^{2-}$ complex of slightly distorted tetrahedral symmetry, which would result in a structured absorption band for the electronic transitions type $^1A_1 \rightarrow {}^1T_2$. Ding et al [65] have established that the blue emissions are caused by $^1A_1 \rightarrow {}^1T_2$electronic transitions in groups of intrinsic tetrahedra $[MoO_4]^{2-}$ and green emissions by structural defects of the Frenkel type exist on the surface layer of the crystals.

The origin and the mechanisms responsible for the photoluminescence emissions of molybdates are not yet fully understood. Several hypotheses supported by experimental and theoretical results are reported in the literature to explain this optical property. Campos et al [66], through theory calculations, propose that the $CaMoO_4$ particles emission processes may be related to the existence of distorted groups $[MoO_3]$

and [MoO_4] in the lattice. These authors have argued that these groups lead to the formation of localized levels of energy in the band gap. Marques et al. [67] associate the dependence of photoluminescent properties with the structural order disorder of molybdate prepared by the polymeric precursor method. Ryu et al. [68] verified that both the degree of crystallization and morphology are two important factors in the photoluminescence emissions of $BaMoO_4$ particles, while Sczancoski et al. [35] suggest that the nature of these emissions are very dependent on the local atomic organizations in the structure.

Insert Figure 8

Figure 8. Photoluminescence emission spectra of the particles (a) $ZnMoO_4$, and $ZnMoO_4$: 1% Tb^{3+}, 1% Tm^{3+}, x Eu^{3+} % mol: (b) x= 1%, (c) x= 1.5%, (d) x= 2%, (e) x= 2.5% and (f) x= 3% mol; detail of quenching effect on transition $^5D_0 \rightarrow {}^7F_2$ (Eu^{3+})

Insert Figure 9

Figure 9. Deconvolutions of the photoluminescence emission spectra of the particles (a) $ZnMoO_4$; $ZnMoO_4$: 1% Tb^{3+}, 1% Tm^{3+}, x Eu^{3++} % mol: (b) x= 1%, (c) x= 1.5%, (d) x= 2%, (e) x= 2.5% and (f) x= 3% mol

Figure 8 shows the emission bands for specific RE^{3+}transitions. For Tb^{3+}, they are$^5D_4 \rightarrow {}^7F_j$ (J= 6, 5) located at 490 and 546 nm, respectively. The typical transitions of Eu^{3+} $^5D_0 \rightarrow {}^7F_j$ (J = 1,2 and 4) are positioned at 590, 619 and 624, 702 nm, respectively, while the bands located at 619 and 624 can be attributed to the $^5D_4 \rightarrow {}^7F_2$ (Eu^{3+}) transition. Speghini et al. [69 a] proposed that the transitions are dependent on the symmetry of the sites in which the Eu^{3+} is positioned.

The $^5D_0 \rightarrow {}^7F_1$ transition of Eu^{3+} is a magnetic dipole transition. Its intensity is not influenced by the symmetry of the site. The $^5D_0 \rightarrow {}^7F_2$ transition is known as hypersensitive transition and it is greatly influenced by the local symmetry of the Eu^{3+} cation and the nature of the host matrix. As a consequence, Eu^{3+} dopants can also be used as sensitive probes of local structural symmetry [70]. The asymmetric ratio (R) was calculated considering the ratio between the integrals of the areas under curves $^5D_0 \rightarrow {}^7F_2$ and $^5D_0 \rightarrow {}^7F_1$, according to equation (3), to investigate the symmetry environment of the Eu^{3+}cation site.

$$R = \frac{I(5D0 \rightarrow 7F2)}{I(5D0 \rightarrow 7F1)} \quad (3)$$

The calculated *R* was 1.70. It is observed that the peak of emission of electric dipole at 619 nm dominates the peak of emission of magnetic dipole at 590 nm, which is mainly due to the occupation of Eu^{3+} cations without symmetry inversion [71].

The introduction of the RE^{3+} in the $ZnMoO_4$ favors the photoluminescence emissions as it is observed in Figure 8. For concentrations higher than that one of the sample $ZnMoO_4$: 1% Tb 1% Tm 2% mol Eu^{3+}, a significant drop in intensity can be sensed. This effect is related to a critical concentration which is known as the quenching concentration (see details in Figure 8). In this critical concentration the distance RE^{3+}-RE^{3+} is reduced, which favors the emergence of non-radioactive transitions by a process of cross relaxation [72]. Non-radioactive transitions are expressed in phonon forms, which result in vibrations within the crystal lattice. Wang [73] states that the concentration of the dopant determines the average distance between the two neighboring activator cations as well as the photoluminescence efficiency of RE^{3+} in doped systems.

A decrease in the emission intensity shows the occurrence of energy migration between RE^{3+}in different sites in the lattice, resulting in concentration quenching. Thus, an optimum concentration for $RE^{3+}$is found to be 4 mol% (X_C = 0.04). The concentration quenching occurs by the non-radiative migration of energy between the RE^{3+}catons. The migration of non-radiative energy can take place from two distinct mechanisms: i.e (i) Forster resonance energy transfer (multipole–multipole interaction) and (ii) Dexter mechanism (exchange interaction) [74].

For the Forster resonance energy transfer to be characterized in a system it is necessary that: the donor (**D**) is in the excited state and that the distance between the donor and the activator ion (**A**) is a factor of great influence for the transfer power. The specific conditions must be fulfilled for this mechanism to take place. Note the following points: (I) the emission range of **D** is partially superimposed on the absorption range of **A**, and (II) the distance (**Rc**) between **D** and **A** must be sufficiently short, since the energy transfer efficiency is proportional to $\frac{1}{Rc^6}$, to allow the interaction of the multipole-multipole emission bands of material [75, 76]. The Forster resonance energy transfer can usually happen at distances of up to 100 Å. Dexter (also known as exchange or coalitional energy transfer) is another dynamic quenching mechanism. Dexter energy

transfer is a short-range phenomenon (Rc = 10 Å) that decreases with $e^{-R}$and depends on spatial overlap of donor and quencher molecular orbitals [74].

The critical energy transfer distance (Rc) for $ZnMoO_4$:RE^{3+} was estimated by equation (4) suggested by Blasse [77] from the parameters of the structure, namely the unit cell volume (V), the number of units of the molecular formula per unit cell (Z) and the quenching concentration (Xc).

$$Rc \approx 2[\frac{3V}{4Xc\pi Z}]^{1/3} \quad (4)$$

For the $ZnMoO_4$ system: 1% Tb 1% Tm 2% molEu^{3+}, the following values were considered: Z = 6, V = 564.9384 $Å^3$ and Xc = 0.04, the calculated Rc was 16.50 Å. Normally, the exchange interaction is preferably in an energy transfer process when the value of Rc is between 5 and 10 Å [78]. In case of values higher than 10 Å, there is no indication of exchange interaction in this mechanism. Consequently, other multipolar electrical interactions are responsible for the quenching effect between two more activating ions (RE^{3+}).

To characterize the light emitted by the $ZnMoO_4$ and $ZnMoO_4$:RE^{3+} particles, the chromaticity coordinates (Xc, Yc) were calculated as the basis for the distribution of the photoluminescence emission spectrum as established by the international commission on illumination (CIE) [79,80]. As well as, the correlative color temperature (CCT) of each sample was estimated using McCamy's empirical formula [81].

$$CCT = -449n^3 + 3525n^2 - 6823n + 5520.33 \quad (5)$$

where$n = \frac{(x-xe)}{(y-ye)}$ is the inverse slope line, *xe*= 0.332 and *ye* = 0.

The color reproduction index (CRI) is a quantity that measures the ability of a light source to reveal the colors of various objects faithfully compared to an ideal or natural light source. This index ranges from 0 - 100%, the closer to 100% the greater the color accuracy of objects. Figure 10 represents the chromaticity diagram representing the points of the CIE coordinates (Xc, Yc) of all samples. Table 2 shows the CIE, CCT and CRI coordinates of the $ZnMoO_4$and $ZnMoO_4$:RE^{3+} particles.

Insert Figure 10

Figure 10. Chromaticity diagram.

Table 2. CIE, CCT and CRI coordinates of $ZnMoO_4$ and $ZnMoO_4$: RE^{3+} samples.

Code	Samples	(Xc, Yc)	CCT (K)	CRI	Color
A	$ZnMoO_4$	(0.51, 0.43)	2256	87	Orange
B	$ZnMoO_4$: 1% Tb 1% Tm 1% mol Eu^{3+}	(0.53, 0.41)	1953	84	
C	$ZnMoO_4$: 1% Tb 1% Tm 1.5% mol Eu^{3+}	(0.54, 0.41)	1876	84	
D	$ZnMoO_4$: 1% Tb 1% Tm 2% mol Eu^{3+}	(0.52, 0.42)	2099	93	
E	$ZnMoO_4$: 1% Tb 1% Tm 2.5% mol Eu^{3+}	(0.54, 0.40)	1818	81	
F	$ZnMoO_4$: 1% Tb 1% Tm 3% mol Eu^{3+}	(0.55, 0.42)	1861	82	

The decay was recorded for $^5D_0 \rightarrow {}^7F_2$ transition of Eu^{3+} at 614 nm emission. The decay curves of all the $ZnMoO_4$: RE^{3+} samples exhibited bi-exponential decay as shown in Figure 11 and have been fitted into exponential equation (6). The average lifetime for the bi-exponential decay was calculated from the following formula (7), the calculated decay parameters are listed in table 3.

$$\mathbf{I = A_1 exp^{(\frac{-t}{\tau_1})} + A_2 exp^{(\frac{-t}{\tau_2})}} \qquad (6)$$

Where I is the emission intensity at any time ''τ'' after switching off the excitation illumination, A_1, A_2 are constant. τ_1, τ_2 are the bi-exponential component of the decay time. The average lifetime for 614 nm emission can be determined by the following formula (6):"

$$\boldsymbol{\tau = \frac{(A_1.\tau_1^2) + (A_2.\tau_2^2)}{A_1.\tau_1 + A_2.\tau_2}} \qquad (7)$$

Insert Figure 11

Figure 11: Decay Curves of $ZnMoO_4$ and and $ZnMoO_4$: RE^{3+}

Table 3: Comparison of Emission Lifetimes of ZnMoO4 and and $ZnMoO_4$: RE^{3+}

Samples	λ_{exc} (nm)	λ_{em} (nm)	A_1	τ_1 (ms)	A_2	τ_2 (ms)	τ (ms)
$ZnMoO_4$	394	614	79.87	0.15	230.29	0.50	0.47
$ZnMoO_4$: 1% Tb 1% Tm 1% mol Eu^{3+}	394	614	1054.57	0.70	655.03	0.21	0.62
$ZnMoO_4$: 1% Tb 1% Tm 1.5% mol Eu^{3+}	394	614	384.89	0.31	522.19	0.89	0.77
$ZnMoO_4$: 1% Tb 1% Tm 2% mol Eu^{3+}	394	614	1251.93	0.28	722.74	0.03	0.26
$ZnMoO_4$: 1% Tb 1% Tm 2.5% mol Eu^{3+}	394	614	620.42	0.09	1260.92	0.63	0.59
$ZnMoO_4$: 1% Tb 1% Tm 3% mol Eu^{3+}	394	614	985.03	0.65	488.45	0.08	0.62

And the energy transfer efficiency from host to RE $^{3+}$ can be calculated according to the equation (8) [82]:

$$\mathbf{n} = \left(\mathbf{1} - \frac{\boldsymbol{\tau}}{\boldsymbol{\tau_0}}\right)\mathbf{x}\ \mathbf{100}\% \qquad (8)$$

Where τ and τ_0 is the corresponding emission lifetimes of the donor in the presence and absence of the acceptor (RE^{3+}) for the same donor concentration, respectively. The energy transfer efficiency from the host to RE^{3+} in $ZnMoO_4$ is 43% for sample of $ZnMoO_4$: 1% Tb^{3+} 1% Tm^{3+} 2% molEu^{3+}, that exhibited better luminescence

From the FE-SEM images, it was possible to identify the modifications the morphologies of $ZnMoO_4$ and $ZnMoO_4$:RE^{3+}, as well as to estimate the particle size distribution**. Chemical analyzes were performed from the x-ray fluorescence spectroscopy of samples ZnMoO4 and $ZnMoO_4$: 1% Tb^{3+} 1% Tm^{3+} 3% molEu^{3+}„ proving the existence of the elements Zn, Mo, O, Eu, Tm and Tb.**

For the sample of pure $ZnMoO_4$, it is observed that the particles have plate morphologies, according to the measurements specified in Figure 12 (I). A similar morphology is found for the sample of $ZnMoO_4$: 1% Tb^{3+} 1% Tm^{3+} 1% molEu^3. For $ZnMoO_4$: 1% Tb^{3+} 1% Tm^{3+}1.5% molEu^{3+}, it was identified octahedral particles with well defined facets. The $ZnMoO_4$: 1% Tb^{3+} 1% Tm^{3+}2% mol Eu^{3+}particles exhibited two different types of morphology and octahedral and cubic shape can be sensed. Through the detail of Figure 12 (IV), it can be seen the appearance of cubic structures, evidencing the change in the morphology of the particles. The cubic-shaped particles

are most relevant for the sample $ZnMoO_4$: 1% Tb^{3+} 1% Tm^{3+} 2.5% Eu^{3+}, confirming the trend presented in the previous sample. Moreover, it was possible to identify other forms: hexagonal and octahedral shapes. The sample $ZnMoO_4$: 1% Tb^{3+} 1% Tm^{3+} 3% Eu^{3+}presented particles with cubic and hexagonal shapes.

Insert Figure 12

Figure 12. SEM-FEG images for samples $ZnMoO_4$ (I), and $ZnMoO_4$: 1% Tb^{3+}, 1% Tm^{3+}, x Eu^{3+} 3% mol: x = 1% mol (II), x = 1.5% mol (III), x = 2% mol (IV), x = 2.5% mol (V), and x = 3% mol (VI).

It is well known that the control of the particle growth process is complex and very sensitive to the chemical environment and the internal crystalline structures [83]. The precursor type may be selectively adsorbed on specific exposed surface planes, thereby changing the surface energies and then an inhibition of the appearance of some surface particles along the growth process takes place. Huo [84] stated that the crystallographic planes exposed during the crystal growth process will rapidly decrease during the process as a result of the minimization of the surface energy of the small crystals, which eventually disappear or decrease their participation in the generated morphology. Thus, the surface is generally surrounded by planes with lower surface energies, resulting in slower crystal growth [85].

The equilibrium shape of $ZnMoO_4$and $ZnMoO_4$: RE^{3+}crystals can be calculated using the classic Wulff construction, which minimizes the total surface free energy at a fixed volume, and provides a simple relationship between the Esurf of the (hkl) plane and its distance in the normal direction from the center of the crystallite.

Insert Figure 13

Figura 13. Morphology map of (a) $ZnMoO_4$ and (b) $ZnMoO_4$:12.5 % mol Eu^{3+} crystals obtained from Wulff's construction. The values of $E_{surf}$for (120), (011), (001), (201), (100), (220), (111), and (112) surfaces are employed. Surface energy is in J m^{-2}.

The surface structure and energy values for the (120), (011), (001), (201), (220), (100), (111) and (112) surfaces are described in the supplementary information. According to our results, the order of stability is as follows: (120)> (001)> (011) faces in the ideal model. Initially, it was calculated the ideal morphology of $ZnMoO_4$ and $ZnMoO_4$:Eu^{3+} from the Esurf , and it is constituted by 33% (33%) of (120) surface, 23%

(24%) of (001) surface, 22% (24%) of (011) surface, 16% (14%) of (201) surface, and 6% (7%) of (100) surface, being the values in parenthesis for $ZnMoO_4$:12.5% molEu^{3+}.

The available morphologies for both $ZnMoO_4$ and $ZnMoO_4$:12.5% mol Eu^{3+}systems can be obtained modifying the relative values of the surface energies or each surface, as it is shown in Figure 13(a-b). In this map, it is found the experimental morphology obtained for $ZnMoO_4$in the present work, by means of the following paths: from the ideal morphology by increasing and/or decreasing the E_{surf}value of (011), (100), (220) and (001) surfaces as shown in Figure13a. The morphology reported by Jia et al. and Wang et al [86, 87] can be reached following the path from A to C and to C1 paths, respectively. Jia et al. synthesized $ZnMoO_4$ by hydrothermal method in conditions of different template agents and the as-prepared products presented varied morphologies for the same crystalline phase (monoclinic), showing in Fig 13a the corresponding morphology. Wang et al prepared $ZnMoO_4$via a hydrothermal route with the increase in the monomer concentrations and the influence of temperature on the shape of $ZnMoO_4$ was also investigated, reporting a transition from monoclinic to triclinic phase.

The experimental morphology of $ZnMoO_4$:$Eu^{3+}$was reached by increasing the value of E_{surf} for (100)surface to 3.70 J/m^2as illustrated in Figure 13b. It is known that a change of morphologies can occur because of the presence of surfactants, impurities, temperature, synthetic routes and other factors. Furthermore, in this work, it is proposed a theoretical strategy for obtaining a reaction path, assuming the creation and screening of alternative reaction routes (intermediates states), to lead to a desired morphology, as presented in Figure 13(c-d). Therefore, the values of $E_{surf}$from the calculated ideal morphology were used (Figure 13(c-d))to predict the intermediate states to lead to a desired morphology (experimental), and this strategy allows us to rationalize the different reaction paths to pass the corresponding energy barriers and to control the crystal morphologies.

5. Conclusions

Searching for new classes of inorganic materials, which emerge as a promising option in high-performance applications in the field of photoluminescence, has received special attention. Particularly, oxides doped with rare earth (RE^{3+}) elements present high luminous efficiency, long decay time and emissions in their visible region.

In the present work, $ZnMoO_4$ and $ZnMoO_4$: RE $^{3+}$=Tb^{3+} - Tm^{3+} - x Eu^{3+} (x = 1, 1.5, 2, 2.5 and 3 mol %)crystals were successfully synthesized using the sonochemical method. XRD observation revealed good crystallinity of the samples prepared without any impurities. All samples showed light emission in the orange–red region. Experimental results and first-principles calculations show a reduction in Egap values provoked by the structural defects and changes of the electronic structure promoted by the introduction of RE^{3+} in the $ZnMoO_4$ lattice. We have for the first time demonstrated that the sample $ZnMoO_4$: 1% Tb^{3+}, 1% Tm^{3+}, 2% Eu^{3+}, present a larger photoluminescence intensity. At higher concentrations of RE^{3+}, the quenching effect was observed. The structural and band gap relationship points out the possibility of band gap engineering in these materials through composition modulation.

FEG-SEM images revealed that both $ZnMoO_4$ and $ZnMoO_4$:12.5%Eu^{3+}samples exhibited similar morphologies. First-principle calculations, at density functional theory level, were performed to obtain the values of surface energies and relative stability of the (120), (001), (011), (201), and (100) surfaces and Wulff construction is employed to rationalize the crystal morphologies found by FE-SEM images. A complete map of the morphologies available for $ZnMoO_4$ and $ZnMoO_4$:12.5% mol Eu^{3+} is obtained and a possible explanation for the transformation processes is provided in which the experimental and theoretical morphologies can match. The present study provided fundamental knowledge on $ZnMoO_4$,and the method of controlling its color emission. Then, a new strategy for the rational structural design of $ZnMoO_4$:RE^{3+} crystals for optoelectronic applications is presented.

Acknowledgements

The authors gratefully acknowledge the financial support of the Brazilian governmental research funding agencies CAPES, CNPq, FAPESP and INCTMN. J.A. acknowledge Generalitat Valenciana for *PrometeoII*/2014/022, ACOMP/2014/270, and ACOMP/2015/1202, and Ministerio de Economia y Competitividad (Spain) project CTQ2015-65207-P for financially supporting this research. M.C. acknowledges Generalitat Valenciana for the Santiago Grisolia Program 2015/033. We also acknowledge the Servei Informatica, Universitat Jaume I for a generous allotment of computer time.

References:

[1] Y. Yang, X. Li, W. Feng, W. Yang, W. Li, C. Tao, Effect of surfactants on morphology and luminescent properties of $CaMoO_4$: Eu^{3+} red phosphors, Journal of Alloys and Compounds, 509 (2011) 845.

[2] Y. Jin, J. Zhang, Z. Hao, X. Zhang, X., Synthesis and luminescence properties of clew-like $CaMoO_4$:Sm^{3+}, Eu^{3+}, Journal of Alloys and Compounds, 509 (2011) L348.

[3] J.H. Chung, S.Y. Lee, K.B. Shim, S.-Y. Kweon, S.-C. Ur, J.H. Ryu, Blue upconversion luminescence of $CaMoO_4$: Li^+/Yb^{3+}/Tm^{3+} phosphors prepared by complex citrate method, Applied Physics A 108 (2012) 369.

[4] J. Fei, Q. Sun, J. Li, Y. Cui, J. Huang, W. Hui, H. Hu, Synthesis and electrochemical performance of α-$ZnMoO_4$ nanoparticles as anode material for lithium ion batteries, Materials Letters 198 (2017) 4–7.

[5] W.N. Wang, Y. Kaihatsu, F. Iskandar, K. Okuuama, Highly Luminous Hollow Chloroapatite Phosphors Formed by a Template-Free Aerosol Route for Solid-State Lighting, Chemistry of Materials 21 (2009) 4685.

[6] E.F. Schubertand, J.K. Kim, Solid-state light sources getting smart, Science 308 (2005) 1274.

[7] A.A. Talin, K.A. Dean, J.E. Jaskie, Field emission displays: a critical review, Solid-State Electronics 45 (2001) 963

[8] B.V. Ratnam, M. Jayasimhadri, Kiwan Jang, H.S. Lee, Y. Soung-Soo, J.H. Jeong, White Light Emission from $NaCaPO_4$:Dy^{3+} Phosphor for Ultraviolet-Based White Light-Emitting Diodes, Journal of the American Ceramic Society 93 (2010) 3857.

[9] O.S. Wolfbeis, Lanthanide Luminescence, Springer, New York, 2011.

[10] B.G. Wybourne. Optical Spectroscopy of Lanthanides, CRC Press, Taylor and Francis, Boca Raton, USA, 2007

[11] B.P. Maheshwary, J. Singh, R.A. Singh. Luminescence properties of Eu^{3+} activated $SrWO_4$ nanophosphors-concentration and annealing, RSC Adv. 4 (2015) 32605.

[12] X. Li, Y. Zhang, D. Geng, J. Lian, G. Zhang, Z. Hou, J. Lin. $CaGdAlO_4:Tb^{3+}/Eu^{3+}$ as promising phosphors for full-color field emission displays, J. Mater. Chem. C 2 (2014) 9924.

[13] R. S. Ningthoujam, Enhancement of Luminescence by Rare Earth Ions Doping in Semiconductor Host, ed. S. B. Rai and Y. Dwivedi, Nova Science Publishers Inc., 6 (2012) 145–182.

[14] N. Jaina , B. P. Singhb , R. K. Singha , J. Singha, R.A. Singh. Enhanced photoluminescence behaviour of Eu^{3+} activated $ZnMoO_4$ nanophosphors via Tb^{3+} co-doping for light emitting diode, Journal of Luminescence 188 (2017) 504–513.

[15] A. Pandey, V.K. Rai, V. Kumar, V. Kumar, H.C. Swart, Upconversion based temperature sensing ability of Er^{3+}–Yb^{3+} codoped $SrWO_4$: an optical heating phosphor, Sens. Actuators B 209 (2015) 352.

[16] J.A. Dorman, J.H. Choi, G. Kuzmanich, J.P. Chang, High-Quality White Light Using Core–Shell $RE^{3+}:LaPO_4$ (RE = Eu, Tb, Dy, Ce) Phosphors, J. Phys. Chem. C 116 (2012) 12854.

[17] B.P. Singh, A.K. Parchur, R.S. Ningthoujam, A.A. Ansari, P. Singh, S.B. Rai. Enhanced photoluminescence in $CaMoO_4:Eu^{3+}$ by Gd^{3+} co-doping, Dalton Trans. 43 (2014) 4779.

[18] Y. Jin, J. Zhang, S. Lu, H. Zhao, X. Zhang, X.J. Wang, Fabrication of Eu^{3+} and Sm^{3+} Codoped Micro/Nanosized $MMoO_4$ (M = Ca, Ba, and Sr) via Facile Hydrothermal Method and Their Photoluminescence Properties through Energy Transfer, J. Phys. Chem. C 1125860 (2008).

[19] M. Yang, Y. Liang, Q. Gui, B. Zhao, D. Jin, M. Lin, L. Yan, H. You, L. Dai, Y. Liu, Multifunctional luminescent nanomaterials from $NaLa(MoO_4)_2:Eu^{(3+)/}Tb^{(3+)}$ with tunable decay lifetimes, emission colors, and enhanced cell viability.Sci. Rep. 5 (2015) 11844

[20] F. Wang, X. Liu, Upconversion multicolor fine-tuning: visible to near-infrared emission from lanthanide-doped $NaYF_4$ nanoparticles, J. Am. Chem. Soc. 130 (2008) 5642.

[21] N. Niu, P. Yang, F. He, X. Zhang, S. Gai, C. Li, Lin, Tunable multicolor and bright white emission of one-dimensional $NaLuF_4:Yb^{3+}$, Ln^{3+} (Ln = Er, Tm, Ho, Er/Tm, Tm/Ho) microstructures, J. Mater. Chem. 22 (2012) 10889.

[22] V. Ya. Degoda, Ya. P. Kogut, I. M. Moroz, F. A. Danevich, Long time phosphorescence in $ZnMoO_4$ crystals. Journal ofLuminescence181(2017)269–276.

[23] V. Ya. Degoda, Ya. P. Kogut, I. M. Moroz, F. A. Danevich, Thermally stimulated luminescence in $ZnMoO_4$ crystals. Journal of Luminescence 183 (2017) 424–432.

[24] V. Ya. Degodaa, Ya. P. Koguta, I. M. Moroza, F.A. Danevichb, S.G. Nasonovc, E.P. Makarovc, V.N. Shlegelc, Temperature dependence of luminescence intensity in $ZnMoO_4$ crystals. Materials Research Bulletin 89 (2017) 139–149.

[25] D. Spassky, V. Nagirnyi, S. Vielhauer, H. Mägi, S.G. Nasonov, V.N. Shlegel, A. Belsky, Emission centers in $ZnMoO_4$: Influence of growth conditions and decay Characteristics. Optical Materials 59 (2016) 66–69.

[26] M.A. Patel, B.A. Bhanvase, S.H. Sonawane, Production of cerium zinc molybdate nano pigment by innovative ultrasound assisted approach. Ultrasonics Sonochemistry 20 (2013) 906–913.

[27] Z. Shahri, M. Bazarganipour, M. Salavati-Niasari, Controllable synthesis of novel zinc molybdate rod-like nanostructures via simple surfactant-free precipitation route. Superlattices and Microstructures 63 (2013) 258–266

[28] C. C. Mardare, D. Tanasic, A. Rathner, N. Muller and A.W. Hassel, Growth inhibition of Escherichia coli by zinc molybdate with different crystalline structure. Phys. Status Solidi A 213 (2016) 1471–1478.

[29] L. Wan, J. Shen, Y. Zhang, X. Li, Novel ZnMoO4/reduced graphene oxide hybrid as a high-performance anode material for lithium ion batteries. Journal of Alloys and Compounds 708 (2017) 713-721.

[30] S. Dutta, S. Som, S.K. Sharma, Luminescence and photometric characterization of K^+ compensated $CaMoO_4$:Dy^{3+} nanophosphors, Dalton Transactions 42 (2013) 9654.

[31] W. Reichelt, T. Weber, T. Söhnel, S. Däbritz, Mischkristallbildung im System $CuMoO_4/ZnMoO_4$, Z. Anorg. Allg. Chem. 626 (2000) 2020–2027.

[32] T. Söhnel, W. Reichelt, H. Oppermann, H.j. Mattauch, A. Simon, Zum System Zn/Mo/O. I. Phasenbestand und Eigenschaften der ternären Zinkmolybdate; Struktur von $Zn_3Mo_2O_9$, Z. Anorg. Allg. Chem. 622 (1996) 1274.

[33] K. Pavani, A. Ramanan, Influence of 2-aminopyridine on the formation of molybdates under hydrothermal conditions, Eur. J. Inorg. Chem. 2005 (2005) 3080–3087.

[34] V. B. Mikhailik, H. Kraus, D. Wahl, H. Ehrenberg, M. S. Mykhayl, Optical and luminescence studies of ZnMoO4 using vacuum ultraviolet synchrotron readiation. Nucl. Instrum. Method Phys. Res. A, 562 (2006) 513.

[35] J.C. Sczancoski, L.S. Cavalcante, N.L. Marana, R.O. da Silva, R.L. Tranquilin, M.R. Joya, P.S. Pizani, J.A. Varela, J.R. Sambrano, M. Siu Li, E. Longo, J. Andrés, Electronic structure and optical properties of BaMoO4 powders, Current Applied Physics 10 (2010) 614.

[36] L. S. Cavalcante, J.C. Sczancoski, M. Siu Li, E. Longo and J. A. Varela. β-ZMO microcrystals synthesized by the surfactant-assisted hydrothermal method: Growth process and photoluminescence properties. Colloids and Surfaces A: Physicochem. Eng. Aspects. 396 (2012) 346.

[37] X. JU, X. LI, W. LI, W. YANG, C. TAO, Luminescence properties of ZMO:Tb^{3+} green phosphor prepared via co-precipitation. Materials Letters 65 (2011) 2642.

[38] P. Li, L. Pang, Z. Wang, Z. Yang, Q. Guo, X. Li, Luminescent characteristics of $LiBaBO_3$:Tb^{3+} green phosphor for white LED, J Alloys Compd. 478 (2009) 813.

[39] J. Llanos, R. Castillo, W. Alvarez. Preparation, characterization and luminescence of a new green-emitting phosphor: Gd_2TeO_6 doped with Tb^{3+}. Mater Lett 62 (2008) 3597.

[40] X. Li, Z. Yang, L. Guan, Q. Guo. A new yellowish green luminescent material $SrMoO_4$:Tb^{3+} . Mater Lett. 63 (2009) 1096.

[41] T. Chengaiah, C.K.A. Jayasankar, K. Pavani, T. Sasikala and L.R. Moorthy. Preparation and luminescence characterization of Zn(1-x)MoO_4:xDy^{3+} phosphor for white light-emitting diodes. Optics Communications 312 (2014) 233.

[42] W. Ran, L. Wang, W. Zhang, F. Li, H. Jiang, W. Li, L. Su, R. Houzong, X. Pana, and J. Shi. A super energy transfer process based S-shaped cluster in ZMO phosphors: theoretical and experimental investigation. J. Mater. Chem. C 3 (2015) 8344.

[43] C.T. Lee, W.T. Yang, R.G. Parr. Development of the Colle-Salvetti correlation-energy formula into a functional of the electron density, Phys. Rev. B: Condens. Matter, 37 (1988) 785-789.

[44] A.D. Becke. Perspective on “Density functional thermochemistry. III. The role of exact exchange”, J. Chem. Phys, 98 (1993) 5648-5652.

[45] R. Dovesi, R. Orlando, A. Erba, C.M. Zicovich-Wilson, B. Civalleri, S. Casassa, et al. CRYSTAL14: A program for the ab initio investigation of crystalline solids. International Journal of Quantum Chemistry. 114 (2014) 1287-317.

[46] Access to the site: http://www.crystal.unito.it/Basis_Sets/europium.html.

[47] F.Corà, A.Patel, N.M. Harrison, C.Roetti, C. R.A. Catlow. An ab-initio Hartree-Fock study of alpha-MoO_3, J. Mater. Chem., 7 (1997) 959-967.

[48] C. Gatti, V.R. Saunders, C. Roetti, Crystal field effects on the topological properties of the electron density in molecular crystals: The case of urea, J. Chem. Phys. 101 (1994) 10686-10696

[49] T. Homann, U. Hotje, M. Binnewies, A. Borger, K.D. Becker, T. Bredow. Composition-Dependent Band Gap in ZnSxSe1-x: A Combined Experimental and Theoretical Study, Solid State Science 8 (2006) 44-49.

[50] H.J. Monkhorst, J.D. Pack. Special points for Brillouin-zone integrations

Physical review B, 13 (1976) 5188

[51] G.Wulff. Xxv. zur frage der geschwindigkeit des wachsthums und der auflösung der krystallflächen. Zeitschrift für Kristallographie, Crystalline Materials, 34 (1901) 449-530

[52] M. Bomio, R. Tranquilin, F. V. Motta, C.A. Paskocimas, R. M. Nascimento, L. Gracia, J. Andrés, E. Longo. Towards Understanding the Photocatalytic Activity of $PbMoO_4$ Powders with Predominant (111), (100), (011), and (110) facets. A Combined Experimental and Theoretical Study, The Journal of Physical Chemistry C. 117 (2013) 21382–21395.

[53] M.T. Fabbro, C. Saliby, L.R. Rios, F.A. La Porta, L. Gracia, M. S. Li. Identifying and Rationalizing the Morphological, Structural, and Optical Properties of beta-Ag2MoO4 Microcrystals, and the Formation Process of Ag Nanoparticles on Their Surfaces: Combining Experimental Data and First-Principles Calculations, Sci. Technol. Adv. Mater. 16 (2015) 65002-65011.

[54] M. C. Oliveira et al., On the morphology of $BaMoO_4$ crystals: A theoretical and experimental approach. Crystal Research and Technology, 51 (2016) 634-644.

[55] H.P. Klug, L.E. Alexander, X-Ray Diffraction Procedures, 1959. New York.

[56] Y. Gao, Y. Sun, H. Zou, Y. Sheng, X. Zhou, B. Zhang, B. Zhou, Effect of Eu^{3+} doping on the structural and photoluminescence properties of cubic $CaCO_3$, Mater. Sci. Eng. B 203 (2016) 52.

[57] Y. S. Vidya, K.S. Anantharaju, H. Nagabhushana, S.C. Sharma, H.P. Prashantha, C. Shivakumara, C. Combustion synthesized tetragonal ZrO_2:Eu^{3+} nanophosphors: Structural and photoluminescence studies, Spectrochimica Acta Part A: Molecular and Biomolecular Spectroscopy, 135 (2015) 241–251.

[58] A. Kokalj. Computer graphics and graphical user interfaces as tools in simulations of matter at the atomic scale, Comp. Mater. Sci., 28 (2003) 155.

[59] D.L. Wood and J. Tauc. Weak absortion tails in amorphous semiconductors. Phys. Rev. B., 5 (1972) 3144.

[60] R. Lacomba-Perales, J. Ruiz-Fuertes, D. Errandonea, D. Martınez-Garcıa, A. Segura, Optical absorption of divalent metal tungstates: Correlation between the band-gap energy and the cation ionic radius, Eur. Phys. Lett. 83 (2008) 37002.

[61] I.L. Validzic, T.D. Savic, R.M. Krsmanovic, D.J. Jovanovic, M.M. Novakovic, M.C. Popovic, M.I. Comor, Synthesis, strong room-temperature PL and

photocatalytic activity of ZnO/$ZnWO_4$ rod-like nanoparticles. Mater. Sci. Eng. B. 177 (2012) 645.

[62] J. Ruiz-Fuertes, S. Lopez-Moreno, J. Lopez-Solano, D. Errandonea, A. Segura, R. Lacomba-Perales, A. Munoz, S. Radescu, P. Rodriguez-Hernandez, M. Gospodinov, L.L. Nagornaya, C.Y. Tu, Pressure effects on the electronic and optical properties of AWO_4wolframites (A = Cd, Mg, Mn, and Zn): The distinctive behavior of multiferroic $MnWO_4$, Phys. Rev. B. 86 (2012) 125202.

[63] J. Liu, H. Lian, C. Shi, Improved optical photoluminescence by charge compensation in the phosphor system $CaMoO_4:Eu^{3+}$. Optical Materials 29 (2007) 1591.

[64] V.M. Longo, L.S. Cavalcante, R. Erlo, V.R. Mastelaro, A.T. de Figueiredo, J.R. Sambrano, S. de Lazaro, A.Z. Freitas, L. Gomes, N.D. Vieira Jr., J.A. Varela, E. Longo, Strong violet–blue light photoluminescence emission at room temperature in $SrZrO_3$: Joint experimental and theoretical study. Acta Mater. 56 (2008) 2191.

[65] X.Y. Wu, J. Du, H.B. Li, M.F. Zhang, B.J. Xi, H. Fan, Y.C. Zhu, Y.T. Qian, Aqueous mineralization process to synthesize uniform shuttle-like $BaMoO_4$ microcrystals at room temperature. J. Solid State Chem. 180 (2007) 3288.

[66] S.S. Ding, M. Lei, H. Xiao, G. Liu, Y.C. Zhang, K. Huang, C. Liang, Y.J. Wang, R. Zhang, D.Y. Fan, H.J. Yang, Y.G. Wang. Morphology evolution and photoluminescence of barium molybdate controlled by poly (sodium-4-styrenesulfonate) Journal of Hernandes, Appl. Phys. Lett. 91 (2007) 051923. Journal of Alloys and Compounds 579 (2013) 549.

[67] A.B. Campos, A.Z. Simões, E. Longo, J.A. Varela, V.M. Longo, A.T. de Figueiredo, F.S. De Vicente, A.C. Mechanisms behind blue, green, and red photoluminescence emissions in $CaWO_4$ and $CaMoO_4$ powders. Applied physics letters 91 (2017) 051923.

[68] A.P.A. Marques, F.V. Motta, E.R. Leite, P.S. Pizani, J.A. Varela, E. Longo, D.M.A. de Melo, Evolution of photoluminescence as a function of the structural order or disorder in $CaMoO_4$ nanopowders. J. Appl. Phys. 104 (2008) 043505.

[69] J.H. Ryu, J.W. Yoon, C.S. Lim, K.B. Shim, Microwave-assisted synthesis of barium molybdate by a citrate complex method and oriented aggregation. Mater. Res. Bull. 40 (2005) 1468.

[70] A. Speghini and M. Bettinelli. Preparation, structural characterization and luminescence properties of Eu^{3+} - doped nanocrystalline ZrO_2. J. Mater. Res. 20 (2005) 2780-2789.

[71] K. Binnemans. Interpretation of europium(III) spectra, Coordination Chemistry Reviews 295 (2015) 1–45.

[72] M. Inokuti and F. Hirayama. Influence of Energy Transfer by the Exchange Mechanism on Donor Luminescence, Journal of Chemical Physics, 4(1965) 1978.

[73] F. Wang, X.G. Liu. Recent advances in the chemistry of lanthanide-doped upconversion nanocrystals. Chem. Soc. Rev. 38 (2009) 976.

[74] P. Jena, S. K. Gupta, V. Natarajan, M. Sahu, N. Satyanarayana, M. Venkateswarlu. Structural characterization and photoluminescence properties of sol–gel derived nanocrystalline $BaMoO_4$:Dy^{3+}, Journal of Luminescence 158 (2015) 203–210.

[75] G. García-Rosales, et al., Energy transfer from Tb^{3+} to Eu^{3+} ions sorbed on $SrTiO_3$ surface, J. Luminescence 132 (2012) 1299-1306.

[76] L.X. Lovisa, J. Andres, L. Gracia, M.S. Li, C.A. Paskocimas, M.R.D. Bomio V.D. Araujo, E. Longo, F.V. Motta. Photoluminescent properties of ZrO_2: Tm^{3+}, Tb^{3+}, Eu^{3+} powdersd Acombined experimental and theoretical study, Journal of Alloys and Compounds 695 (2017) 3094-3103.

[77] G. Blasse. Energy transfer in oxidic phosphors. Philips Res. Rep. 24 (1969) 131.

[78] F. Kang, Y. Zhang, M. Peng. Controlling the energy transfer via multi luminescent centers to achieve white light/tunable emissions in a single-phased X2-Type Y_2SiO_5: Eu^{3+}, Bi^{3+} phosphor for ultraviolet converted LEDs, Inorg. Chem. 54 (2015) 1462.

[79] E.F. Schubert, Light Emitting Diodes, Cambridge University Press, 2003.

[80] R. Robertson, Computation of correlated color temperature and distribution temperature, J. Opt. Soc. Am. 58 (1968) 1528.

[81] C. S. McCamy. Correlated Color Temperature as an Explicit Function of Chromaticity Coordinates, Wappingers Falls, New York 12590-1804.

[82]P. Boutinaud, L. Sarakha, E. Cavalli, M. Bettinelli, P. Dorenbos, and R. Mahiou, About Red Afterglow in Pr^{3+} Doped Titanate Perovskites, J. Phys. D: Appl. Phys. 42 (2009) 045106–045112.

[83] F.A. La Porta, A.E. Nogueira, L. Gracia, W.S. Pereira, G. Botelho, T.A. Mulinari, J. Andrés and E. Longo. An experimental and theoretical investigation on the optical and photocatalytic properties of ZnS nanoparticles, Journal of Physics and Chemistry of Solids 103 (2017) 179–189.

[84] C.H. Huo, B.S. Wu, P. Gao, Y. Yang, Y.W. Li, H. Jiao. The Mechanism of Potassium Promoter: Enhancing the Stability of Active Surfaces, Angewandte Chemie 123(2011) 7541–7544.

[85] C. Burda, X.B. Chen, R. Narayanan, M.A. El- Sayed. Chemistry and properties of nanocrystals of different shapes, Chemical Reviews. 105 (2005)1025–1102.

[86] R.P. Jia, C. Zhang, J.Y. Xu. Morphology-Controllable Synthesis and Characterization of $ZnMoO_4$ Nanoparticles Advanced Materials Research, 624 (2012) 51-54;

[87] Dongming Wang, Maozhan Huang, Yan Zhuang,Hai-lang Jia, Jianhua Sun, Mingyun Guan. Phase- and Morphology-Controlled Synthesis of Zinc Molybdate for Excellent Photocatalytic Property, Eur. J. Inorg. Chem. 16 (2017) 4939-4946.

Table captions

Table 1. Crystallographic data of $ZnMoO_4$ and $ZnMoO_4$:RE^{3+}samples.

Table 2. CIE, CCT and CRI coordinates of $ZnMoO_4$ and $ZnMoO_4$:RE^{3+}samples.

Table 3: Comparison of Emission Lifetimes of ZnMoO4 and and $ZnMoO_4$: RE^{3+}

Figures captions

Figure 1. X-ray diffraction of the $ZnMoO_4$ materials synthesized by the sonochemical method: (a) $ZnMoO_4$, and $ZnMoO_4$: 1% Tb^{3+}, 1% Tm^{3+}, x Eu^{3+}% mol: (b) x= 1%, (c) x= 1.5%, (d) x= 2%, (e) x= 2.5% and (f) x= 3% mol.

Figure 2. Relationship between crystallite size and microdeformation according to RE^{3+} concentration.

Figure 3. Structural refinement of the samples (a) $ZnMoO_4$, and $ZnMoO_4$: 1% Tb^{3+}, 1% Tm^{3+}, x Eu^{3+} % mol: (b) 1%, (c) 1.5%, (d) 2%, (e) 2.5% and (f) 3% mol.

Figura 4. Theoretical representation of the triclinic 1x2x2 supercell corresponding to (a) $ZnMoO_4$ and (b) $ZnMoO_4$:Eu^{3+} crystals.

Figure 5. Determination of the gap energy value by using the Tauc and Wood method: (a) $ZnMoO_4$ and $ZnMoO_4$: 1% Tb^{3+}, 1% Tm^{3+}, x Eu^{3+}% mol: (b) x= 1%, (c) x= 1.5%, (d) x= 2%, (e) x= 2.5% and (f) x= 3% mol.

Figura 6. Band structure of (a) $ZnMoO_4$ and (b) $ZnMoO_4$:Eu^{3+} crystals.

Figura 7. Projected total DOS of (a) $ZnMoO_4$ and (b) $ZnMoO_4$:Eu^{3+} crystals.

Figure 8. Photoluminescence emission spectra of the particles (a) $ZnMoO_4$, and $ZnMoO_4$: 1% Tb^{3+}, 1% Tm^{3+}, x Eu^{3+} % mol: (b) x= 1%, (c) x= 1.5%, (d) x= 2%, (e) x= 2.5% and (f) x= 3% mol; detail of quenching effect on transition $^5D_0 \rightarrow {}^7F_2$ (Eu^{3+})

Figure 9. Deconvolutions of the photoluminescence emission spectra of the particles (a) $ZnMoO_4$; $ZnMoO_4$: 1% Tb^{3+}, 1% Tm^{3+}, x Eu^{3++} % mol: (b) x= 1%, (c) x= 1.5%, (d) x= 2%, (e) x= 2.5% and (f) x= 3% mol

Figure 10. Chromaticity diagram.

Figure 11: Decay Curves of $ZnMoO_4$ and and $ZnMoO_4$: RE^{3+}

Figure 12. SEM-FEG images for samples $ZnMoO_4$ (I), and $ZnMoO_4$: 1% Tb^{3+}, 1% Tm^{3+}, x Eu^{3+} 3% mol: x = 1% mol (II), x = 1.5% mol (III), x = 2% mol (IV), x = 2.5% mol (V), and x = 3% mol (VI).

Figura 13. Morphology map of (a) $ZnMoO_4$ and (b) $ZnMoO_4$:12.5 % molEu^{3+} crystals obtained from Wulff's construction. The values of E_{surf} for (120), (011), (001), (201), (100), (220), (111), and (112) surfaces are employed. Surface energy is in J m^{-2}.

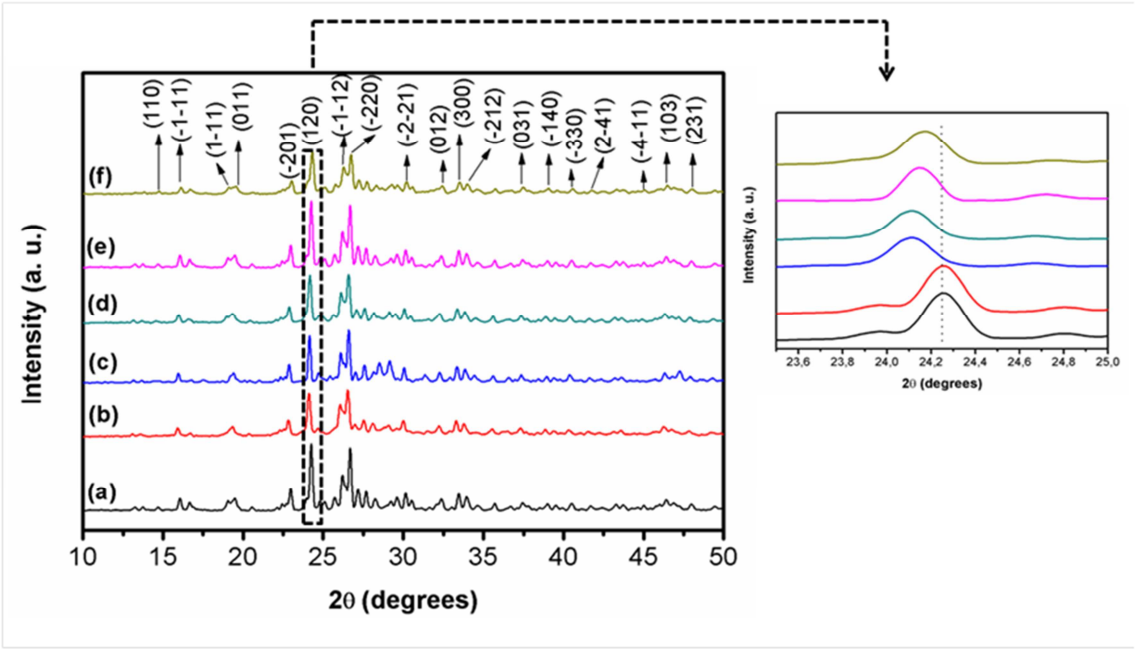

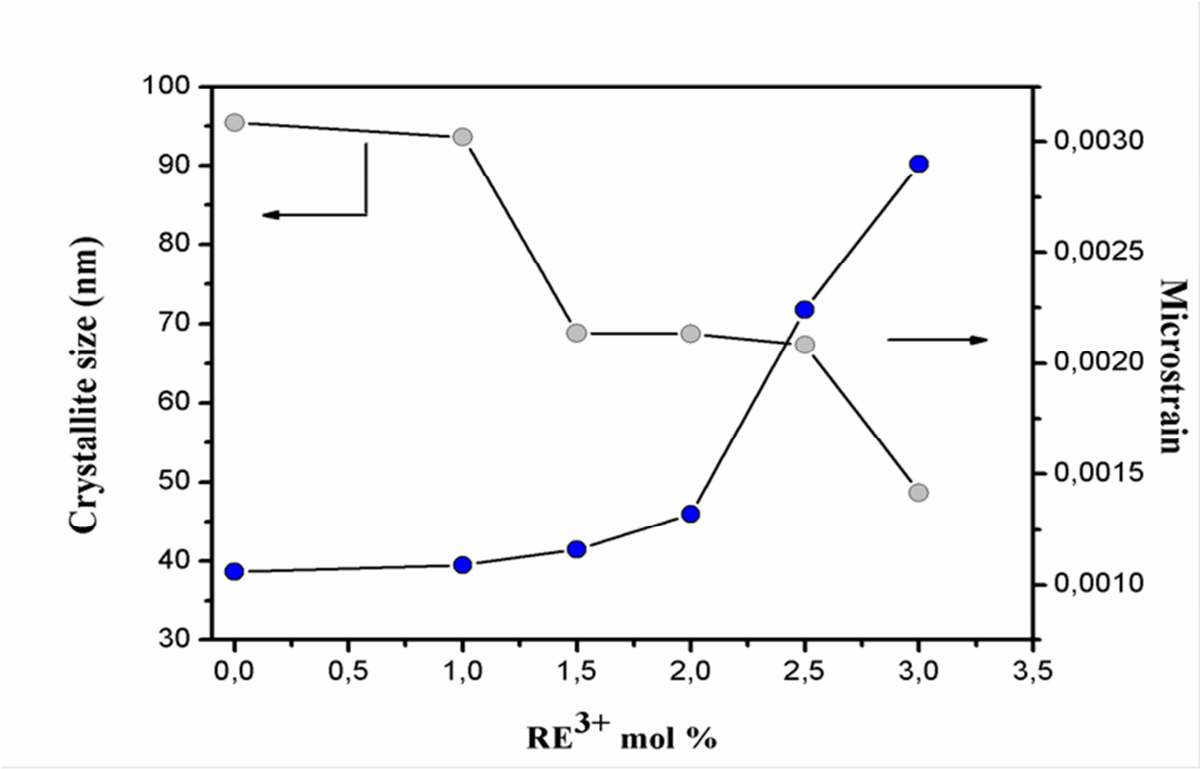

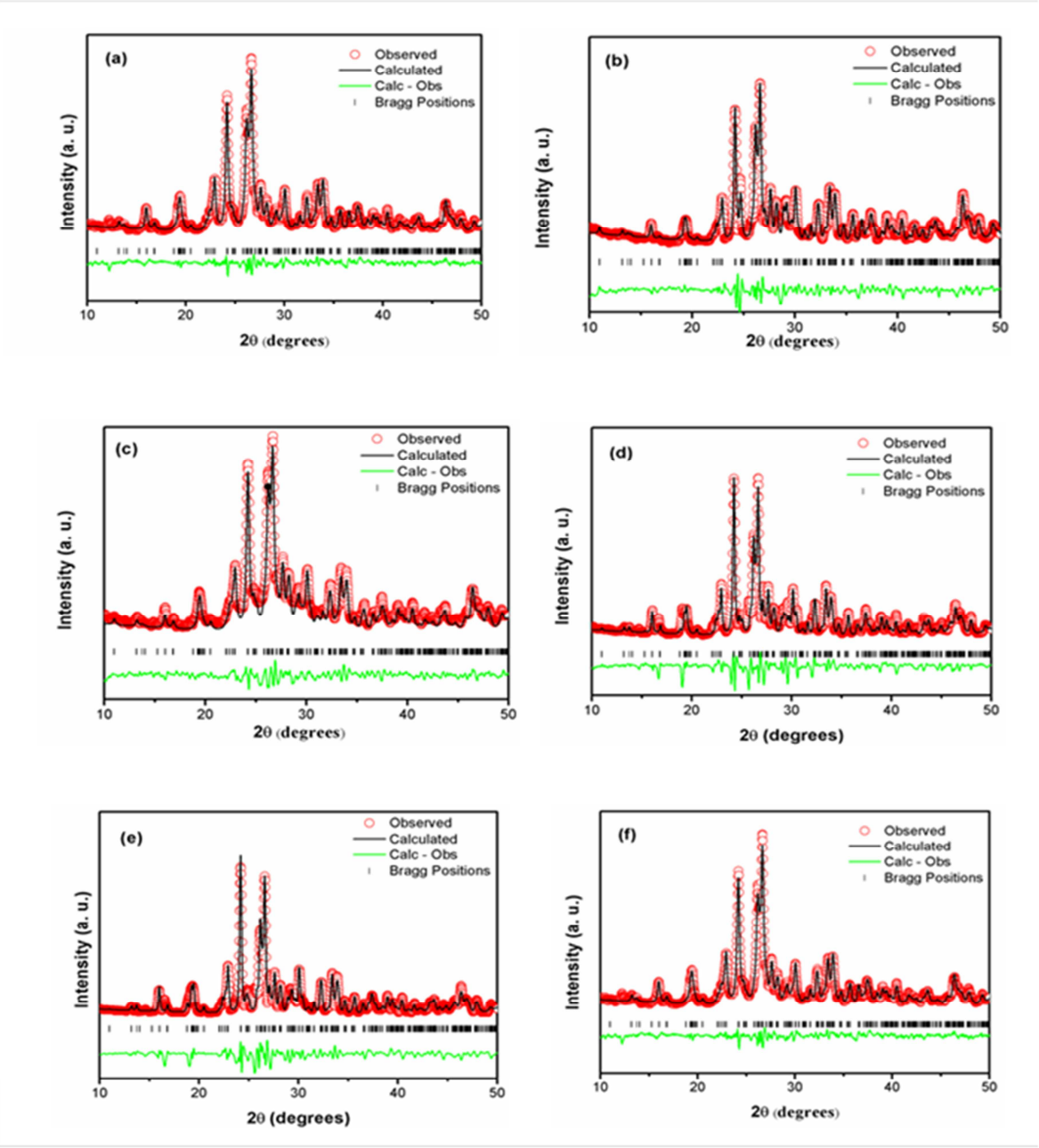

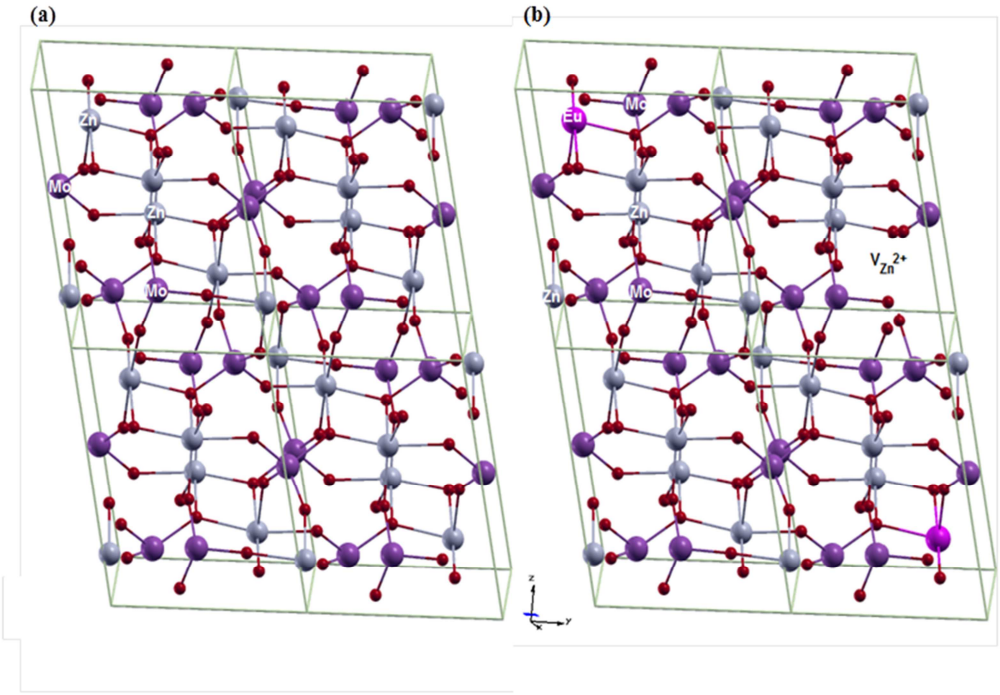

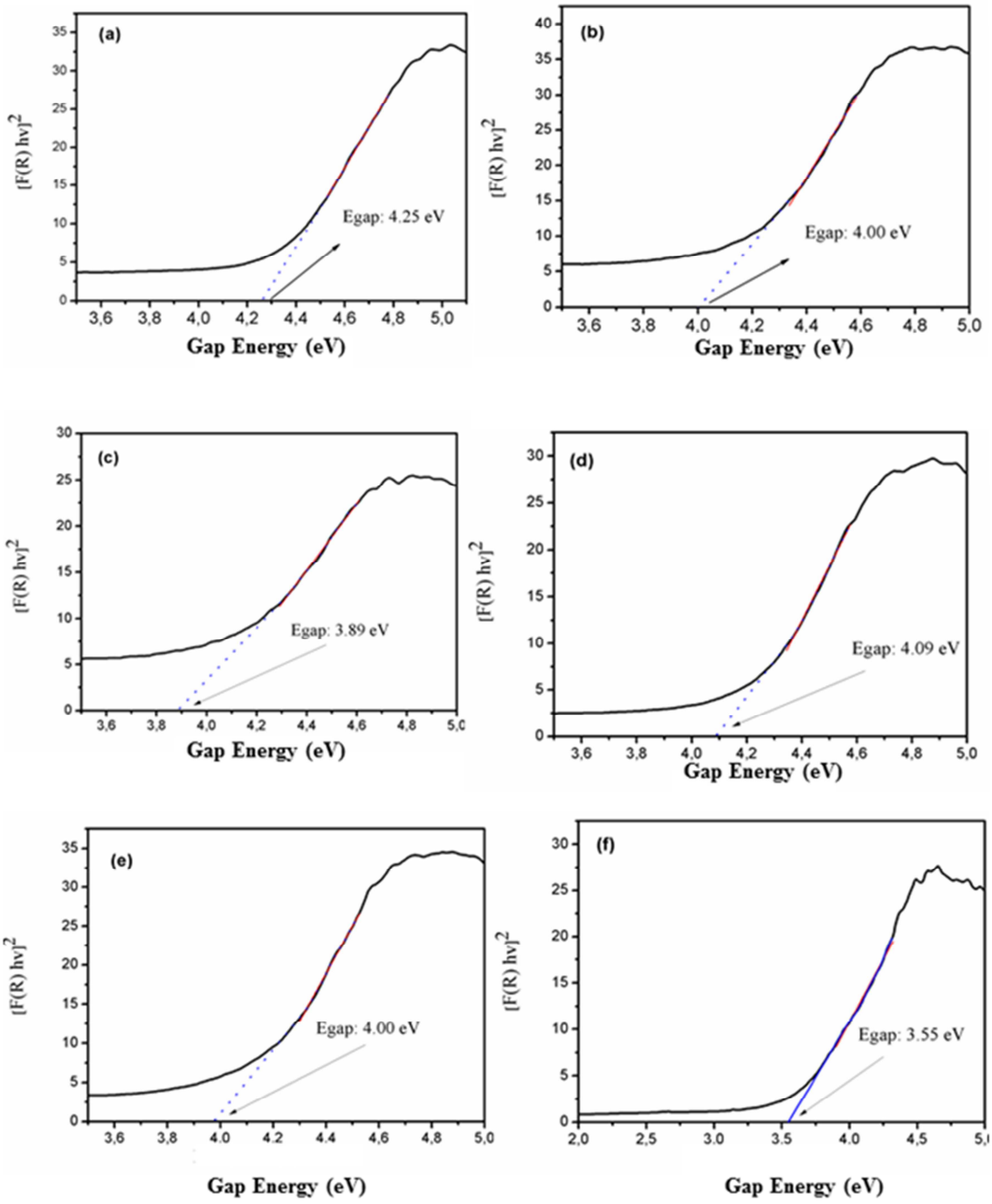
(a)
Egap: 4.25 eV
[F(R) hν]2
Gap Energy (eV)
(b)
Egap: 4.00 eV
[F(R) hν]2
Gap Energy (eV)
(c)
Egap: 3.89 eV
[F(R) hν]2
Gap Energy (eV)
(d)
Egap: 4.09 eV
[F(R) hν]2
Gap Energy (eV)
(e)
Egap: 4.00 eV
[F(R) hν]2
Gap Energy (eV)
(f)
Egap: 3.55 eV
[F(R) hν]2
Gap Energy (eV)

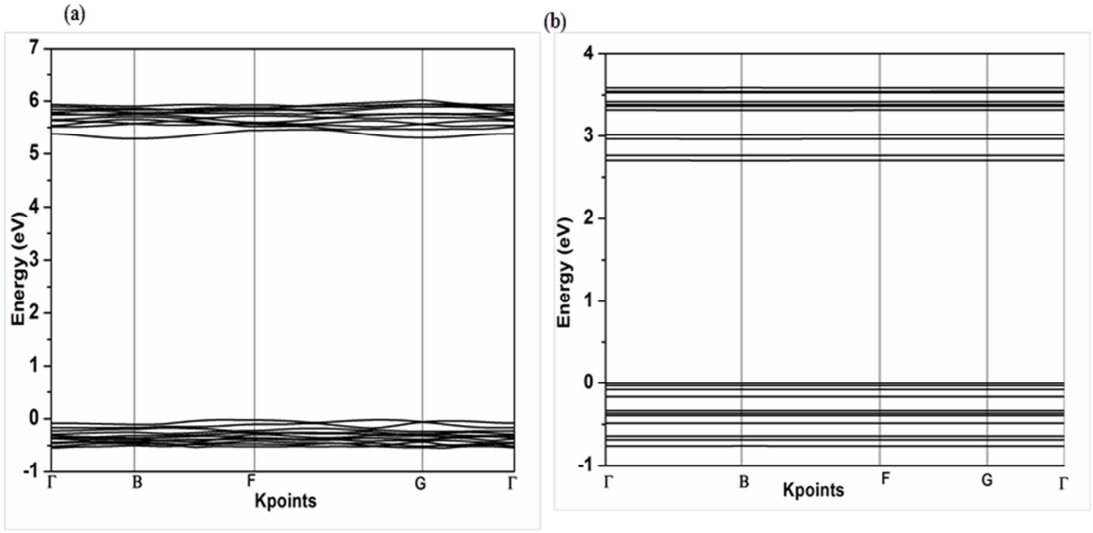

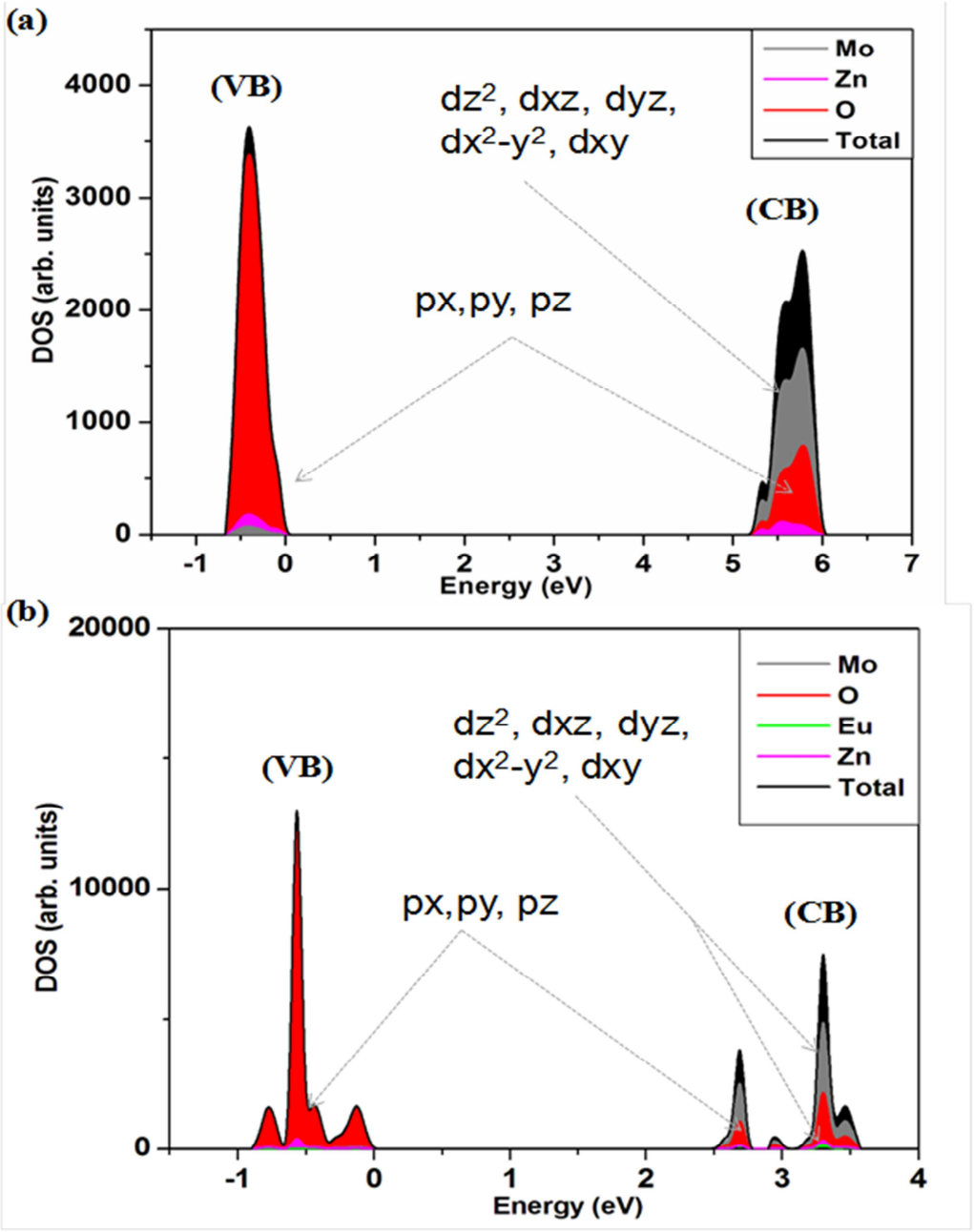
(a)
(VB)
dz2, dxz, dyz,
dx2-y2, dxy
(CB)
px,py, pz
Mo
Zn
O
Total
DOS (arb. units)
Energy (eV)
(b)
(VB)
dz2, dxz, dyz,
dx2-y2, dxy
(CB)
px,py, pz
Mo
O
Eu
Zn
Total
DOS (arb. units)
Energy (eV)

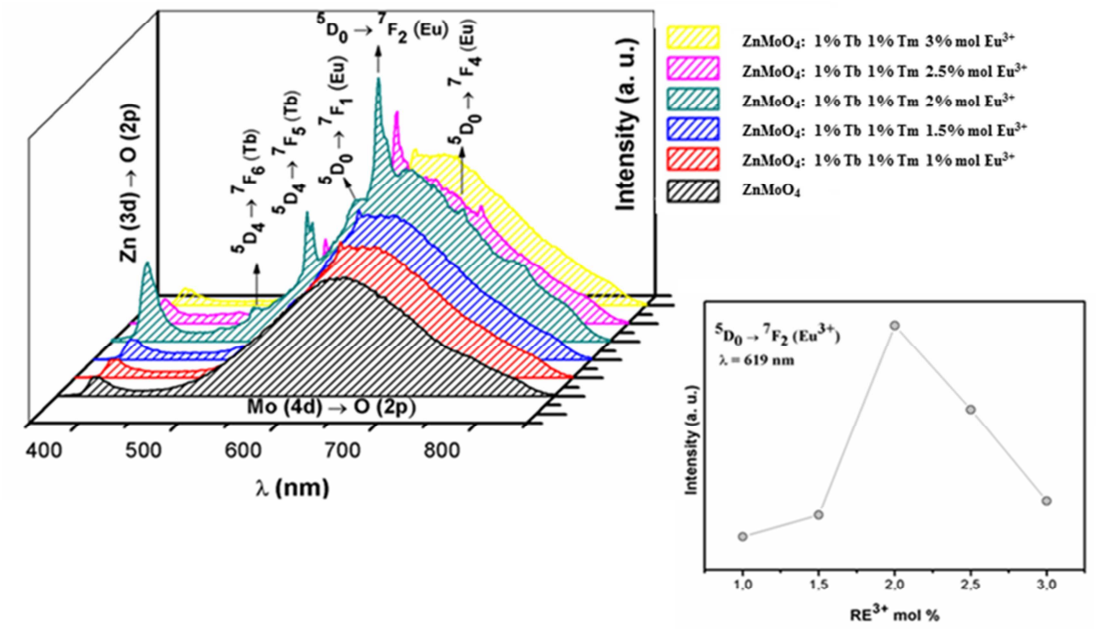

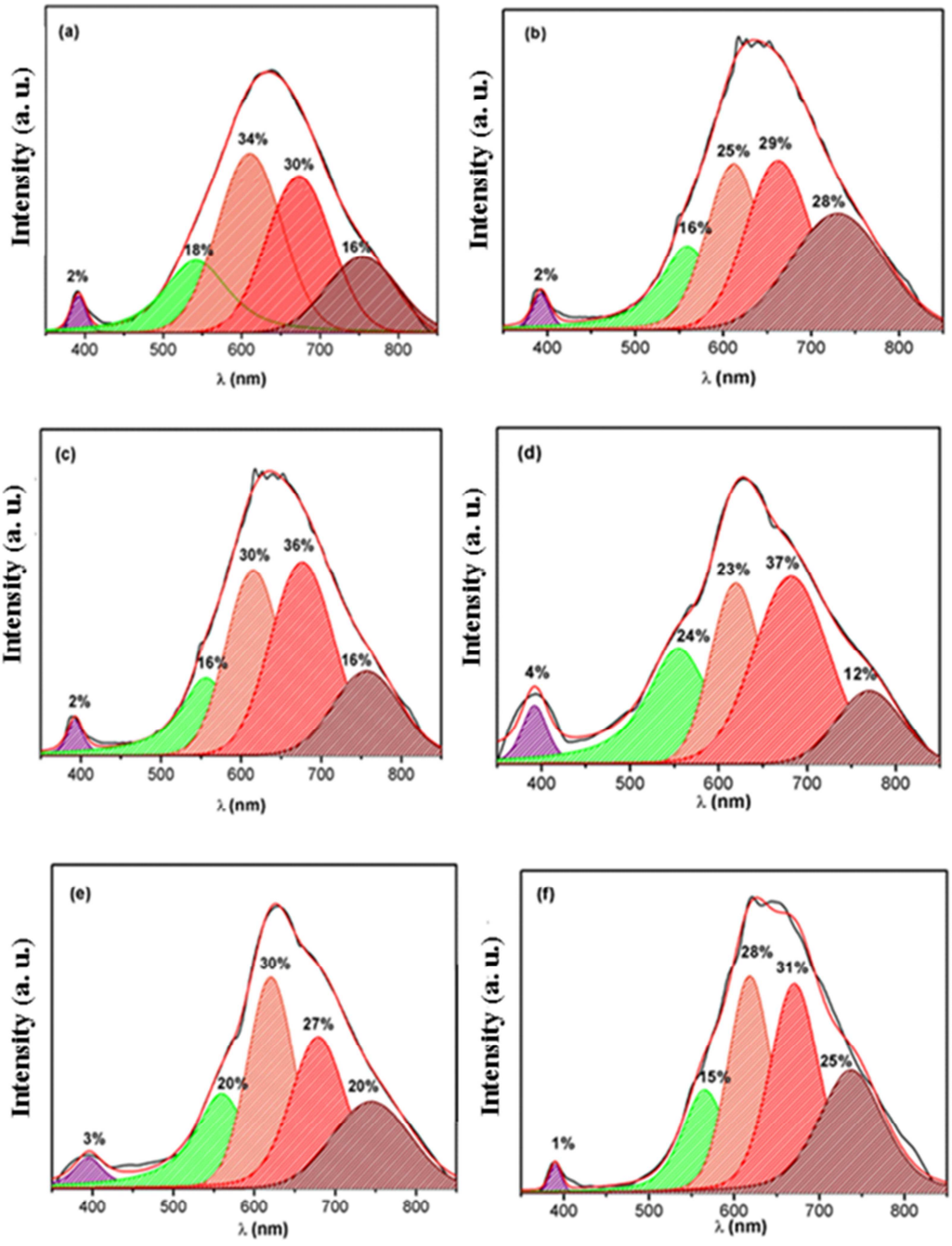
(a)
Intensity (a. u.)
2%
18%
34%
30%
16%
λ (nm)
(b)
Intensity (a. u.)
2%
16%
25%
29%
28%
λ (nm)
(c)
Intensity (a. u.)
2%
16%
30%
36%
16%
λ (nm)
(d)
Intensity (a. u.)
4%
24%
23%
37%
12%
λ (nm)
(e)
Intensity (a. u.)
3%
20%
30%
27%
20%
λ (nm)
(f)
Intensity (a. u.)
1%
15%
28%
31%
25%
λ (nm)

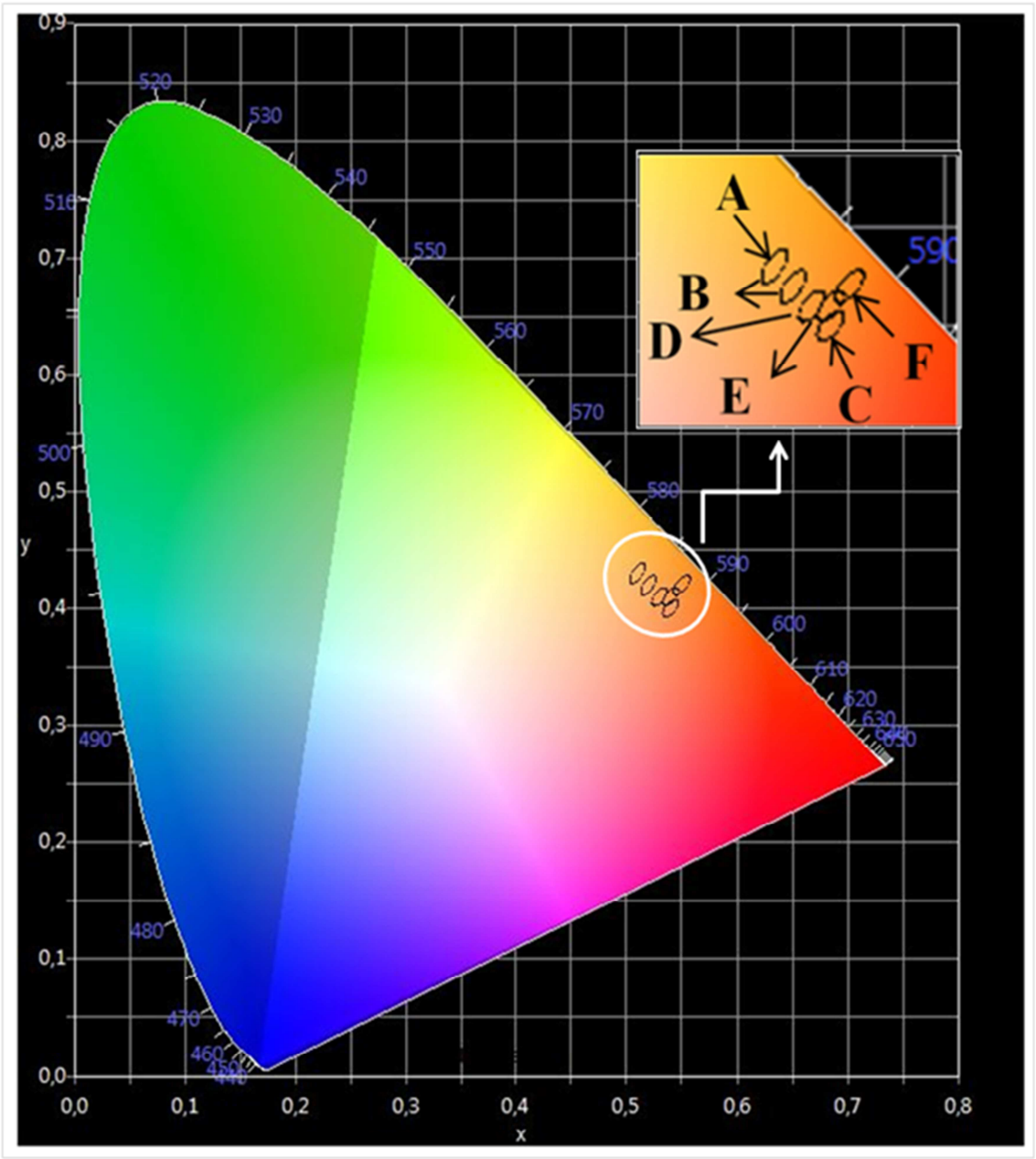
A
B
D
E
C
F
590
x
y
0,0
0,1
0,2
0,3
0,4
0,5
0,6
0,7
0,8
0,9
520
530
540
550
560
570
580
590
600
610
620
630
650
490
480
470
460
500
510

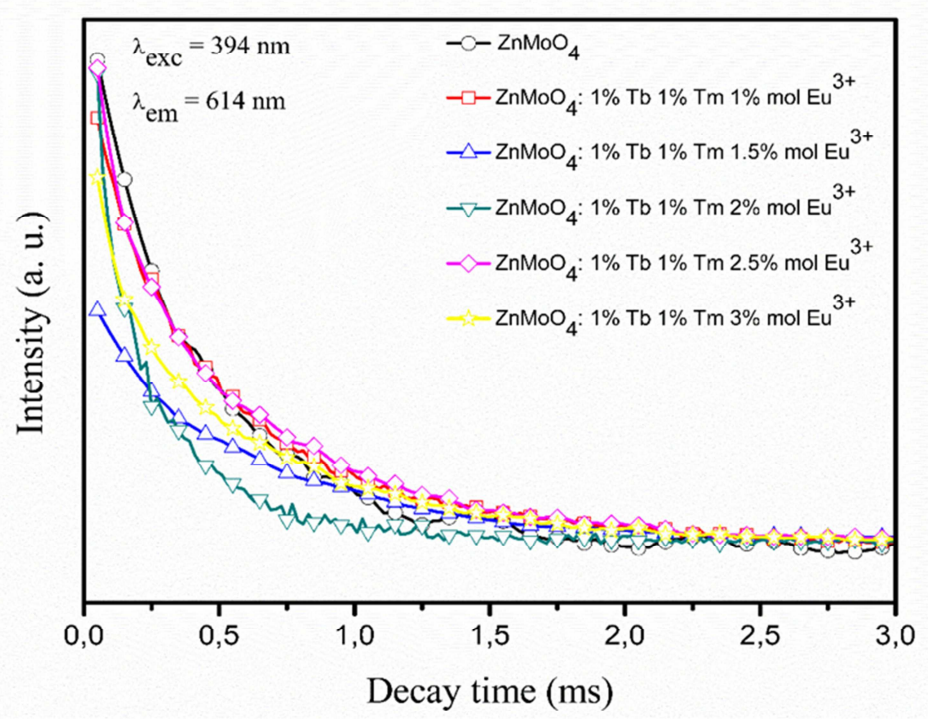

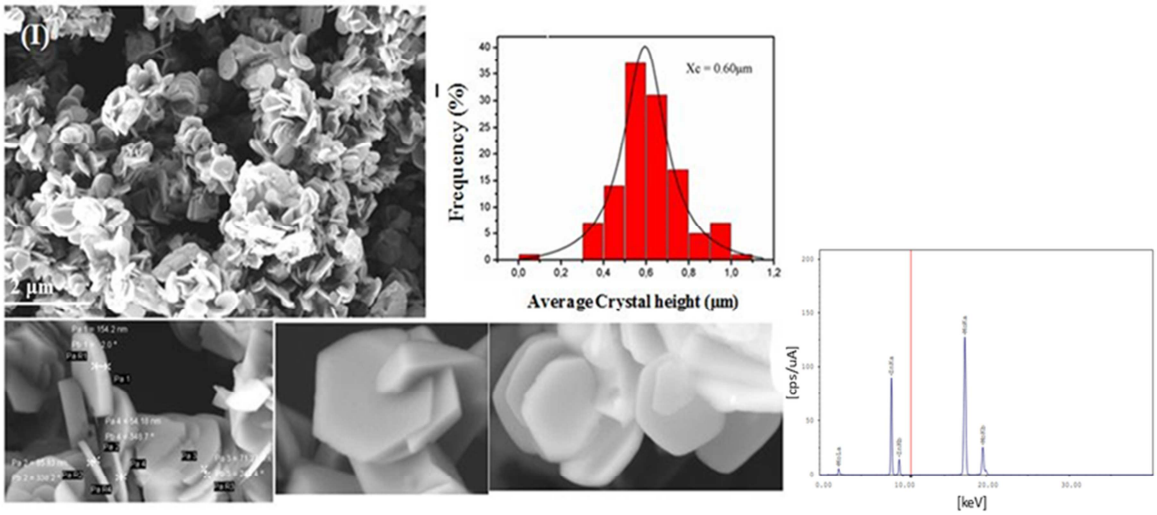

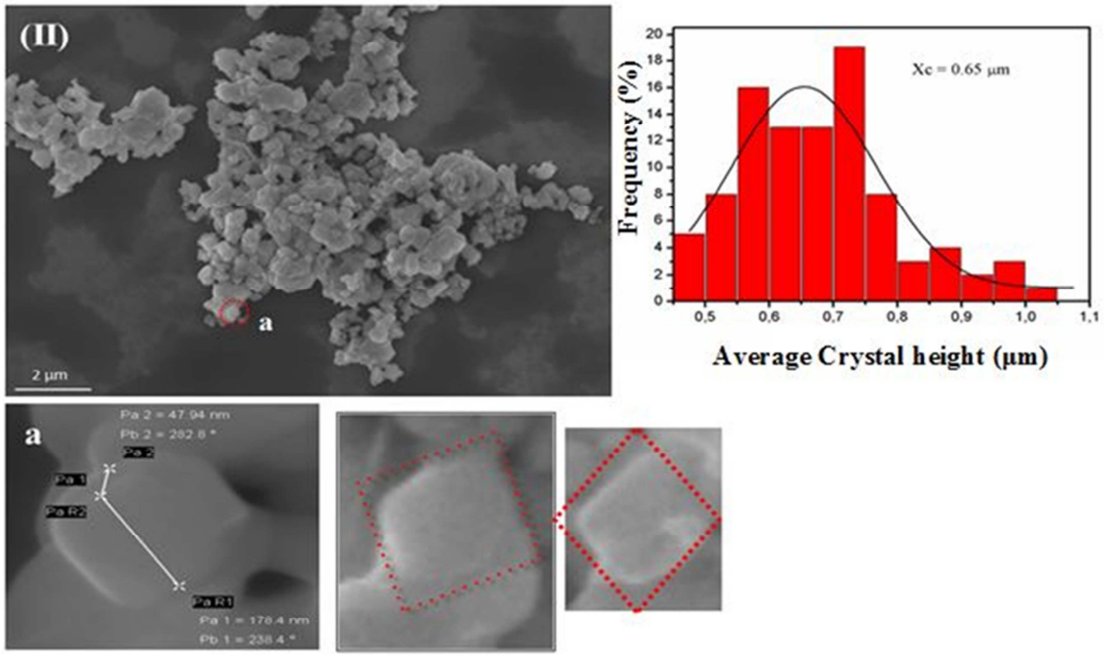

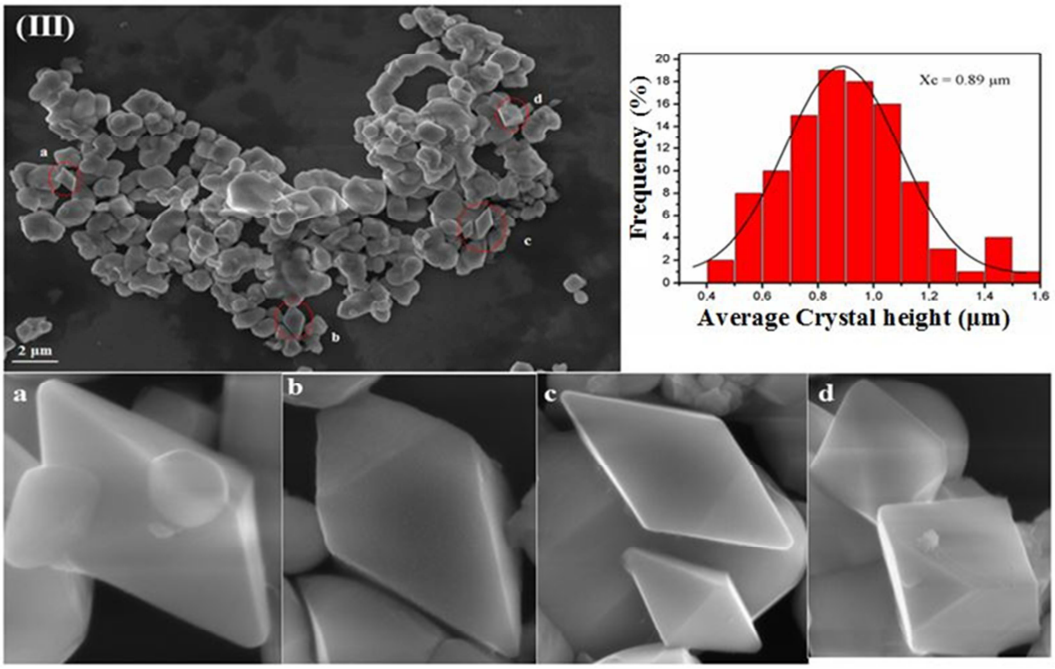

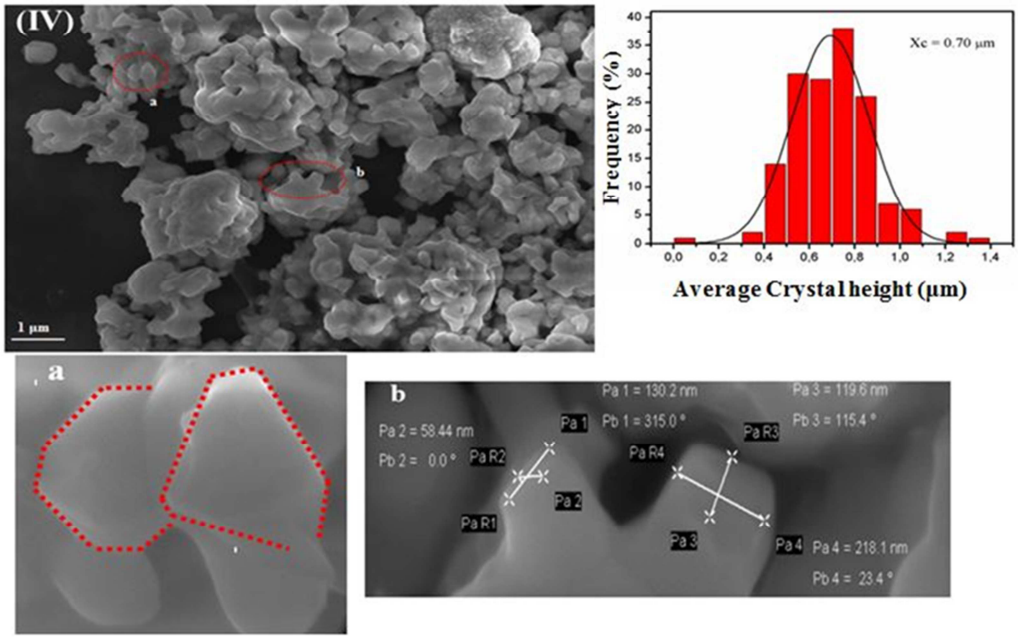

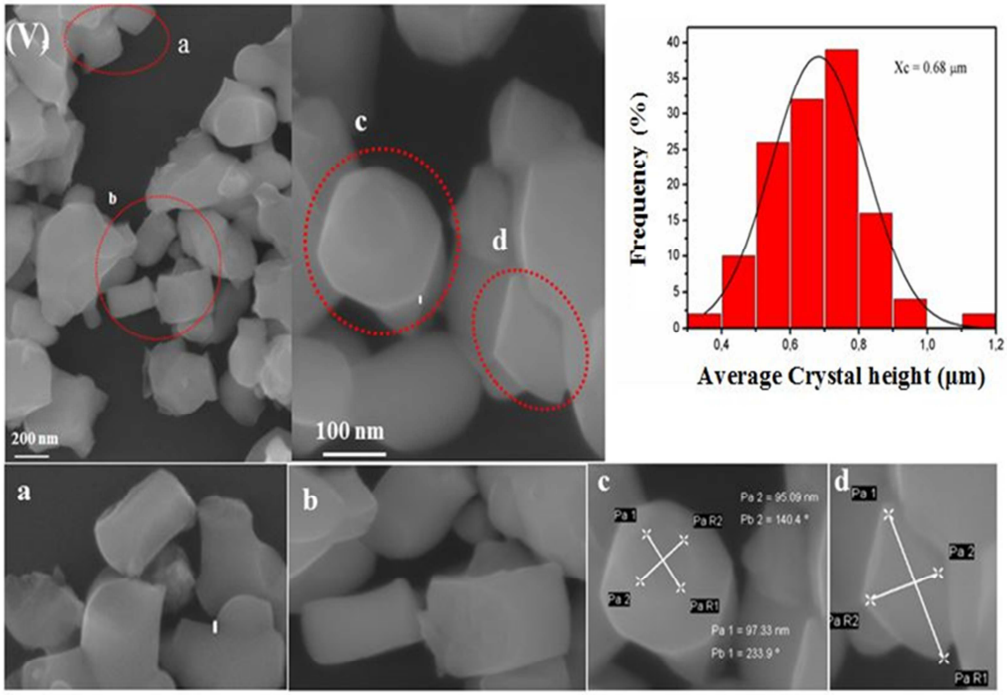

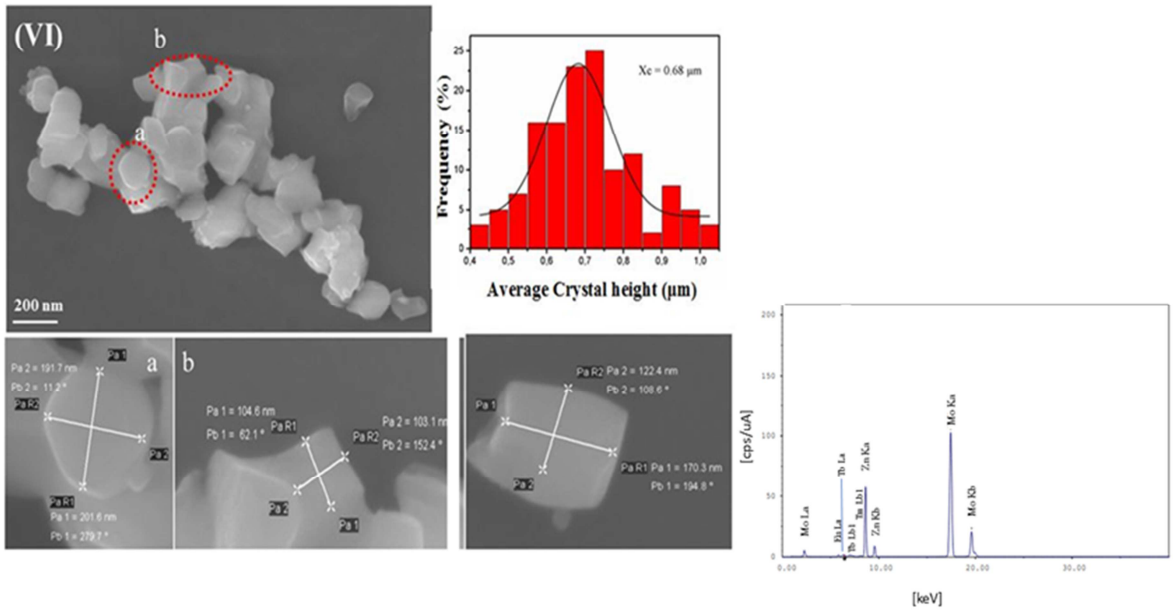

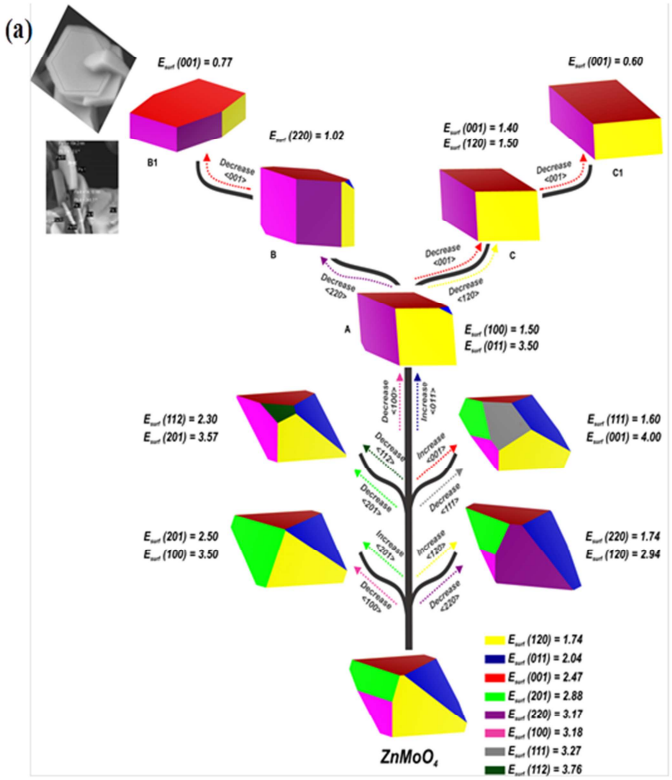

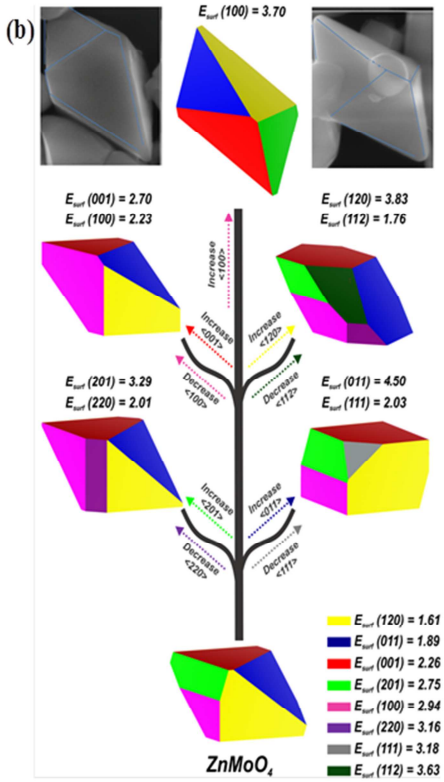

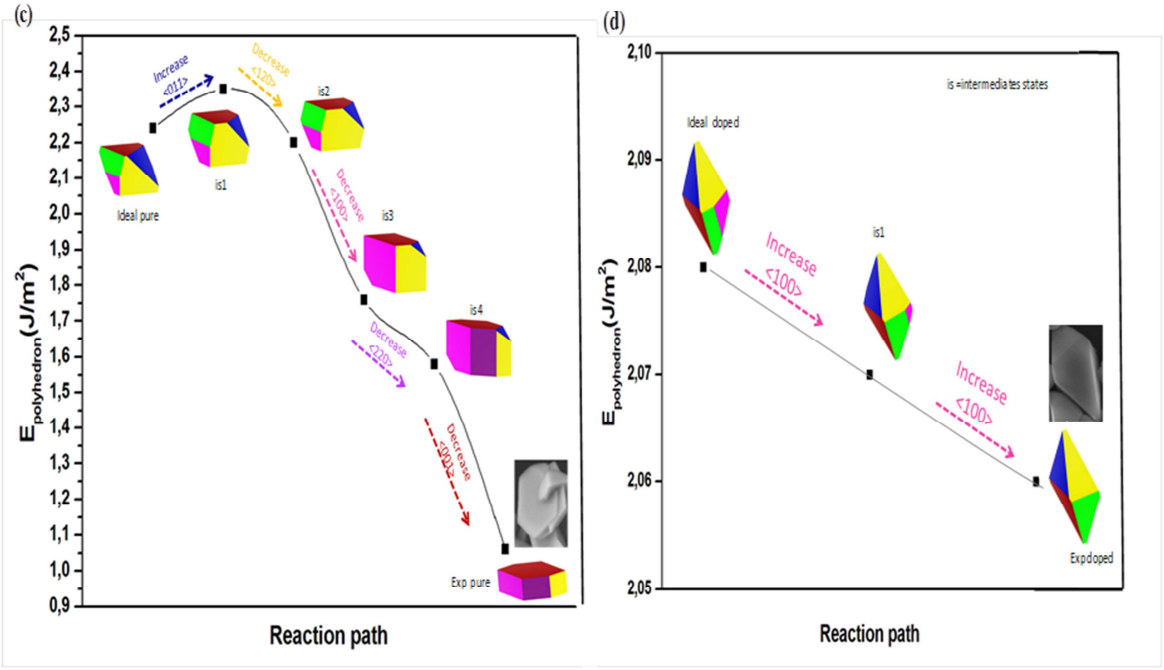

Highlights

- A complete map of the available morphologies of the samples is obtained.
- An explanation has been proposed between experimental and theoretical morphologies.
- A new strategy for the structural design of $ZnMoO_4$: RE^{3+} crystals is presented.
- The α- $ZnMoO_4$ crystals were successfully synthesized using the sonochemical method.
- All samples showed light emission in the orange–red region